



# A hands-on introduction to Physics-Informed Neural Networks for solving partial differential equations with benchmark tests taken from astrophysics and plasma physics

Hubert Baty

## ► To cite this version:

Hubert Baty. A hands-on introduction to Physics-Informed Neural Networks for solving partial differential equations with benchmark tests taken from astrophysics and plasma physics. 2024. hal-04491808

HAL Id: hal-04491808

<https://hal.science/hal-04491808>

Preprint submitted on 6 Mar 2024

**HAL** is a multi-disciplinary open access archive for the deposit and dissemination of scientific research documents, whether they are published or not. The documents may come from teaching and research institutions in France or abroad, or from public or private research centers.

L'archive ouverte pluridisciplinaire **HAL**, est destinée au dépôt et à la diffusion de documents scientifiques de niveau recherche, publiés ou non, émanant des établissements d'enseignement et de recherche français ou étrangers, des laboratoires publics ou privés.

# A hands-on introduction to Physics-Informed Neural Networks for solving partial differential equations with benchmark tests taken from astrophysics and plasma physics

Hubert Baty\*

Observatoire Astronomique, Université de Strasbourg, 67000 Strasbourg, France

March 1, 2024

## Abstract

I provide an introduction to the application of deep learning and neural networks for solving partial differential equations (PDEs). The approach, known as physics-informed neural networks (PINNs), involves minimizing the residual of the equation evaluated at various points within the domain. Boundary conditions are incorporated either by introducing soft constraints with corresponding boundary data values in the minimization process or by strictly enforcing the solution with hard constraints. PINNs are tested on diverse PDEs extracted from two-dimensional physical/astrophysical problems. Specifically, we explore Grad-Shafranov-like equations that capture magnetohydrodynamic equilibria in magnetically dominated plasmas. Lane-Emden equations that model internal structure of stars in self-gravitating hydrostatic equilibrium are also considered. The flexibility of the method to handle various boundary conditions is illustrated through various examples, as well as its ease in solving parametric and inverse problems. The corresponding Python codes based on PyTorch/TensorFlow libraries are made available.

---

\*Corresponding author: [hubert.baty@unistra.fr](mailto:hubert.baty@unistra.fr)

# Contents

|           |   |           |
|-----------|---|-----------|
| <b>1</b>  | <b>Introduction</b>   | <b>3</b>  |
| <b>2</b>  | <b>Physics-Informed Neural Networks</b>   | <b>4</b>  |
| 2.1       | Problem statement for 2D direct problems . . . . .                                  | 4         |
| 2.2       | Problem statement for parametric and inverse problems . . . . .                     | 4         |
| 2.3       | Classical deep learning approach with neural networks using training data . . . . . | 4         |
| 2.4       | PINNs for solving PDEs . . . . .  | 8         |
| 2.5       | Python codes . . . . .  | 10        |
| <b>3</b>  | <b>Laplace equation</b>   | <b>10</b> |
| 3.1       | Using vanilla-PINNs on Dirichlet BCs problem . . . . .                              | 11        |
| 3.2       | Using hard-PINNs on Dirichlet BCs problems . . . . .                                | 12        |
| <b>4</b>  | <b>Poisson equations</b>  | <b>14</b> |
| 4.1       | Using vanilla-PINNs on Dirichlet problems . . . . .                                 | 15        |
| 4.2       | Using vanilla-PINNs on Neumann problems . . . . .                                   | 16        |
| 4.3       | Using vanilla-PINNs on Neumann-Dirichlet problems . . . . .                         | 17        |
| 4.4       | Using vanilla-PINNs on Cauchy problems . . . . .                                    | 17        |
| <b>5</b>  | <b>Helmholtz equations</b>  | <b>18</b> |
| 5.1       | Specific problem related to astrophysics . . . . .                                  | 18        |
| 5.2       | Solutions using vanilla-PINNs with Dirichlet BCs . . . . .                          | 20        |
| 5.3       | More general Helmholtz problems . . . . .   | 20        |
| <b>6</b>  | <b>Grad-Shafranov equations</b>   | <b>20</b> |
| 6.1       | Example of Soloviev equilibrium: the drop-like structure . . . . .                  | 21        |
| 6.2       | Examples of Soloviev equilibria: toroidal fusion devices . . . . .                  | 22        |
| 6.3       | Other examples of more general equilibria in a rectangular domain . . . . .         | 23        |
| <b>7</b>  | <b>Lane-Emden equations</b>   | <b>24</b> |
| 7.1       | A mathematical example . . . . .  | 24        |
| 7.2       | A physical example . . . . .  | 26        |
| <b>8</b>  | <b>Parametric differential equation</b>   | <b>29</b> |
| 8.1       | Parametric solution for stationary advection diffusion in one dimension . . . . .   | 29        |
| 8.2       | Stiff problems involving singular layers . . . . .                                  | 30        |
| <b>9</b>  | <b>Inverse problem differential equation: parameter identification</b>              | <b>32</b> |
| <b>10</b> | <b>Discussion and conclusion</b>  | <b>33</b> |
| <b>11</b> | <b>Appendix</b>   | <b>35</b> |

# 1 Introduction

Since the introduction of Physics-Informed Neural Networks (PINNs) by Raissi et al. (2019), there has been a significant upsurge in interest in the PINNs technique, spanning various scientific fields. Notably, this technique offers several advantages, such as numerical simplicity compared to conventional schemes. Despite not excelling in terms of performance (accuracy and training computing time), PINNs present a compelling alternative for addressing challenges that prove difficult for traditional methods, such as inverse problems or parametric partial differential equations (PDEs). For comprehensive reviews, refer to Cuomo et al. (2022) and Karniadakis et al. (2021).

In this article, I introduce a tutorial on the PINNs technique applied to PDEs containing terms based on the Laplacian in two dimensions (2D), extending the previous tutorial work applied to ordinary differential equations (ODEs) by Baty & Baty (2023). More precisely, I focus on solving different Poisson-type equations called Grad-Shafranov equations and representing magnetic equilibria in magnetically dominated plasmas (e.g. the solar corona), following some examples presented in Baty & Vignon (2024) and also other well known examples (see Cerfon et al. 2011). Additionally, PDEs representative of two dimensional internal star structures are also solved, extending a previous work in a one dimensional approximation (Baty 2023a, Baty 2023b). The latter equations are generally called Lane-Emden equations in the literature. Note that, not only direct problems are considered but also inverse problems for which we seek to obtain an unknown term in the equation. Of course, for these latter problems, additional data on the solutions is required.

I demonstrate how the PINNs technique is particularly well-suited when non Dirichlet-like conditions are imposed at boundaries. This is evident in scenarios involving mixed Dirichlet-Neumann conditions, especially those relevant to the Cauchy problem.

The distinctive feature of the PINNs technique lies in minimizing the residual of the equation at a predefined set of data known as collocation points. At these points, the predicted solution is obligated to satisfy the differential equation. To achieve this, a physics-based loss function associated with the residual is formulated and employed. In the original method introduced by Raissi et al. (2019), often referred to as vanilla-PINNs in the literature, the initial and boundary conditions necessary for solving the equations are enforced through another set of data termed training points, where the solution is either known or assumed. These constraints are integrated by minimizing a second loss function, typically a measure of the error like the mean-squared error. This loss function captures the disparity between the predicted solution and the values imposed at the boundaries. The integration of the two loss functions results in a total loss function, which is ultimately employed in a gradient descent algorithm. An advantageous aspect of PINNs is its minimal reliance on extensive training data, as only knowledge of the solution at the boundary is required for vanilla-PINNs. It's worth noting that, following the approach initially proposed by Lagaris (1998), there is another option to precisely enforce boundary conditions to eliminate the need for a training dataset (see for example Baty 2023b and Urban et al. 2023). This involves compelling the neural networks (NNs) to consistently assign the prescribed value at the boundary by utilizing a well-behaved trial function. The use of this latter second option, also referred as hard-PINNs below, is illustrated in this paper.

This paper is structured as follows. In Section 2, we begin by introducing the fundamentals of the PINNs approach for solving partial differential equations (PDEs). Section 3 focus on the application to solve a simple Laplace equation in a rectangular domain, with the aim to compare the use of vanilla-PINNs versus hard-PINNs on problems involving Dirichlet BCs. The use of PINNs solvers on Poisson equations with different types of BCs in rectangular domains are illustrated in Sect. 4. Section 5 focus on the application to a particular Helmholtz equation, representative of magnetic

arcade equilibrium structures in the solar corona. Another application for computing magnetic structures representative of curved loops is also considered as shown by the obtained solution of Grad-Shafranov equations in Section 6. Section 7 is devoted to another astrophysical problem, that is solving Lane-Emden equations representative of the internal equilibrium structures of polytropic self-gravitating gas spheres (first order approximation for the structure of stars). Finally, the use of PINNs for solving parametric differential equation and inverse problem are illustrated in Section 8 and Section 9 respectively, by considering a stationary advection-diffusion problem. Conclusions are drawn in Section 10.

## 2 Physics-Informed Neural Networks

### 2.1 Problem statement for 2D direct problems

We consider a partial differential equation (PDE) written in the following residual form as,

$$\mathcal{F}(u, x, y, u_x, u_y, \dots) = 0, \quad (x, y) \in \Omega, \quad (1)$$

where  $u(x, y)$  denotes the desired solution and  $u_x, u_y, \dots$  are the required associated partial derivatives of different orders with respect to  $x$  and  $y$ . Specific conditions must be also imposed at the domain boundary  $\partial\Omega$  depending on the problem (see below in the paper).

Note that the  $(x, y)$  space variables can also include non-cartesian coordinates (see Lane-Emden equation).

### 2.2 Problem statement for parametric and inverse problems

We consider a partial differential equation (PDE) written in the following residual form as,

$$\mathcal{F}(u, x, \mu, u_x, \dots) = 0, \quad x \in \Omega, \quad \mu \in \Omega_p, \quad (2)$$

where the desired solution is now  $u(x, \mu)$ , with  $x$  being the space variable associated to the one dimensional domain  $\Omega$  and  $\mu$  is a scalar parameter taking different values in  $\Omega_p$ . For parametric problems,  $\mu$  is treated exactly as a second variable in a 2D direct problem, but for inverse problems  $\mu$  is consequently considered as an unknown. Boundary conditions (BC) are again necessary for parametric problems, but additional conditions, such as knowledge of the solution at some  $x$  values must be added for inverse problems.

Note that, for the sake of simplicity, we have considered only one dimensional space variable in this work for parametric and inverse problems. The extension to higher spatial dimensions is however straightforward.

### 2.3 Classical deep learning approach with neural networks using training data

In the classical deep learning approach with neural networks (NNs), the model is trained exclusively using available training data. This method involves feeding input data into the neural network, which then adjusts its internal parameters through a training process to minimize the difference between predicted and actual output values. The model learns patterns and relationships within the training dataset to make predictions on new, unseen data. This approach is common in various machine learning applications, where the emphasis is on leveraging labeled training examples to achieve accurate predictions. In this way, NNs serve as non-linear approximators.

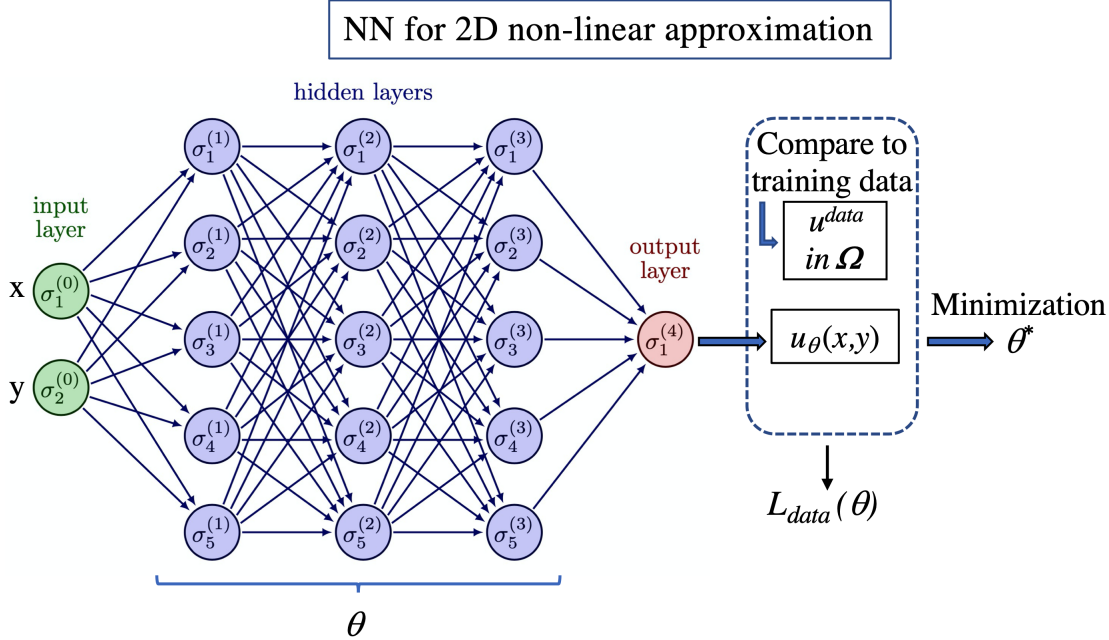


Figure 1: Schematic representation of the structure for a Neural Network (NN) applied to a non-linear approximation problem. The input layer has two input variables (i.e. two neurons) for the two space coordinate variables  $x$  and  $y$ . Three hidden layers with five neurons per layer are connected with the input and the output layer, where the latter has a single variable (one neuron) representing the predicted solution  $u_\theta(x, y)$ . The minimization procedure using the loss function  $L_{\text{data}}(\theta)$  is obtained by comparing  $u_\theta$  to a training data set of values  $u^{\text{data}}$  taken in the 2D domain  $\Omega$ . In this simplified example,  $\theta$  represents a total number of 81 scalar parameters.

**Approximating the solution with a neural network.** For any input  $\mathbf{x}$  representing either the spatial coordinates  $(x, y)$ , or the combination of variables  $(x, \mu)$ , or only  $x$ , depending on the problems, we want to be able to compute an approximation of the solution value  $u(\mathbf{x})$  and eventually the parameter value  $\mu$  (for inverse problems).

For this, we introduce what is called a multi-layer perceptron, which is one of the most common kind of neural networks. Note that any other statistical model could alternatively be used. The goal is to calibrate its parameters  $\theta$  such that  $u_\theta$  approximates the target solution  $u(\mathbf{x})$ .  $u_\theta$  is a non-linear approximation function, organized into a sequence of  $L + 1$  layers. The first layer  $\mathcal{N}^0$  is called the input layer and is simply:

$$\mathcal{N}^0(\mathbf{x}) = \mathbf{x}. \quad (3)$$

Each subsequent layer  $\ell$  is parameterized by its weight matrix  $\mathbf{W}^\ell \in \mathbb{R}^{d_{\ell-1} \times d_\ell}$  and a bias vector  $\mathbf{b}^\ell \in \mathbb{R}^{d_\ell}$ , with  $d_\ell$  defined as the output size of layer  $\ell$ . Layers  $\ell$  with  $\ell \in [1, L - 1]$  are called hidden layers, and their output value can be defined recursively:

$$\mathcal{N}^\ell(\mathbf{x}) = \sigma(\mathbf{W}^\ell \mathcal{N}^{\ell-1}(\mathbf{x}) + \mathbf{b}^\ell), \quad (4)$$

$\sigma$  is a non-linear function, generally called activation function. While the most commonly used one is the ReLU ( $\text{ReLU}(\mathbf{x}) = \max(\mathbf{x}, 0)$ ), we use the hyperbolic tangent  $\tanh$  in this work, which is

more suited than ReLU for building PINNs. The final layer is the output layer, defined as follows:

$$\mathcal{N}^L(\mathbf{x}) = \mathbf{W}^L \mathcal{N}^{L-1}(\mathbf{x}) + \mathbf{b}^L, \quad (5)$$

Finally, the full neural network  $u_\theta$  is defined as  $u_\theta(\mathbf{x}) = \mathcal{N}^L(\mathbf{x})$ . It can be also written as a sequence of non-linear functions

$$u_\theta(\mathbf{x}) = (\mathcal{N}^L \circ \mathcal{N}^{L-1} \dots \mathcal{N}^0)(\mathbf{x}), \quad (6)$$

where  $\circ$  denotes the function composition and  $\theta = \{\mathbf{W}^l, \mathbf{b}^l\}_{l=1,L}$  represents the parameters of the network.

**Supervised learning approach using training data.** The classical supervised learning approach assumes that we have at our disposal a dataset of  $N_{data}$  known input-output pairs  $(\mathbf{x}, u)$ :

$$\mathcal{D} = \{(\mathbf{x}_i^{data}, u_i^{data})\}_{i=1}^{N_{data}},$$

for  $i \in \llbracket 1, N_{data} \rrbracket$ .  $u_\theta$  is considered to be a good approximation of  $u$  if predictions  $u_\theta(\mathbf{x}_i)$  are close to target outputs  $u_i^{data}$  for every data samples  $i$ . We want to minimize the prediction error on the dataset, hence it's natural to search for a value  $\theta^*$  solution of the following optimization problem:

$$\theta^* = \underset{\theta}{\operatorname{argmin}} L_{data}(\theta) \quad (7)$$

with

$$L_{data}(\theta) = \frac{1}{N_{data}} \sum_{i=1}^{N_{data}} |(u_\theta(\mathbf{x}_i) - u_i^{data})|^2. \quad (8)$$

$L_{data}$  is called the loss function, and equation (7) the learning problem. It's important to note that the defined loss function relies on the mean squared error formulation, but it's worth mentioning that alternative formulations are also possible. Solving equation (7) is typically accomplished through a (stochastic) gradient descent algorithm. This algorithm depends on automatic differentiation techniques to compute the gradient of the loss  $L_{data}$  with respect to the network parameters  $\theta$ . The algorithm is iteratively applied until convergence towards the minimum is achieved, either based on a predefined accuracy criterion or a specified maximum iteration number as,

$$\theta^{j+1} = \theta^j - l_r \nabla_{\theta} L(\theta^j), \quad (9)$$

with  $L = L_{data}$ , for the  $j$ -th iteration also called epoch in the literature, where  $l_r$  is called the learning rate parameter. In this work, we choose the well known Adam optimizer. This algorithm likely involves updating the network parameters ( $\theta$ ) iteratively in the opposite direction of the gradient to reduce the loss. The standard automatic differentiation technique is necessary to compute derivatives with respect to the NN parameters, i.e. weights and biases (Baydin et al. 2018). This technique consists of storing the various steps in the calculation of a compound function, then calculating its gradient using the chaine rule. In practice, the learning process is significantly streamlined by leveraging open-source software libraries such as TensorFlow or PyTorch, especially when working with Python. These libraries provide pre-implemented functions and tools for building, training, and optimizing neural network models. TensorFlow and PyTorch offer user-friendly interfaces, extensive documentation, and a wealth of community support, making them popular choices for researchers

### Vanilla-PINN for direct 2D PDE – Dirichlet BCs

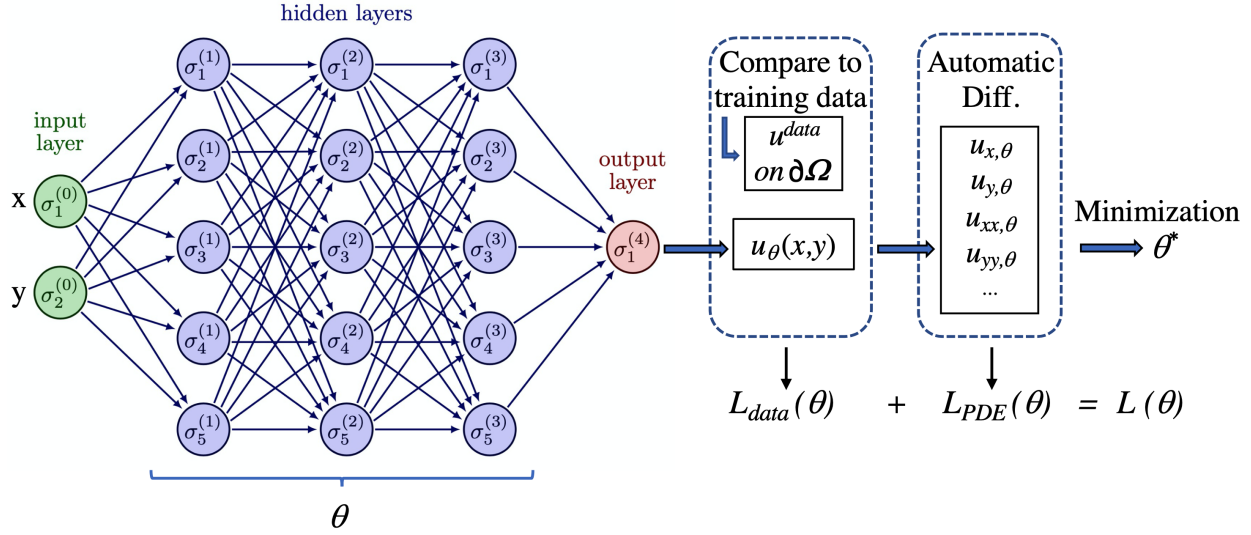


Figure 2: Schematic representation of the structure for a Physics-Informed Neural Network applied for solving a PDE associated to a 2D direct problem with Dirichlet-like BCs (soft constraints). The input layer has two input variables (i.e. two neurons) for the two space coordinate variables  $x$  and  $y$ . Three hidden layers with five neurons per layer are connected with the input and the output layer, where the latter has a single variable (one neuron) representing the predicted solution  $u_\theta(x, y)$ . Automatic Differentiation (AD) is used in the procedure in order to evaluate the partial derivatives (i.e.  $u_{x,\theta}$ ,  $u_{xy\theta}\dots$ ) necessary to form the PDE loss function  $L_{PDE}(\theta)$ . The loss function  $L_{data}(\theta)$  is obtained with soft constraints (i.e. via the training data set) imposed on the boundary domain  $\partial\Omega$ .

and practitioners in the field of deep learning. Note that, in this work TensorFlow library is used for direct problems while PyTorch is preferred for parametric and inverse problems.

A schematic representation of the architecture of a neural network designed to approximate a learned function  $u(x, y)$  with a supervised learning approach using a training data set  $N_{data}$  is visible in Fig. 1. In this case, two input neurons (first layer) represent the two spatial variables, and the output neuron (last layer) is the predicted solution  $u_\theta$ . The intermediate (hidden) layers between the input and output layers where the neural network learns complex patterns and representations, consists of 5 neurons per layer in this example of architecture. The total number of learned parameters is given by the formula  $(i \times h_1 + h_1 \times h_2 + h_2 \times h_3 + h_3 \times o + h_1 + h_2 + h_3 + o)$  that is therefore equal to 81, as  $h_1 = h_2 = h_3 = 5$ ,  $i = 2$  and  $o = 1$  ( $i$  and  $o$  being the number of input and output neurons respectively, and  $h_i$  being the number of neurons of the  $i - th$  hidden layer).

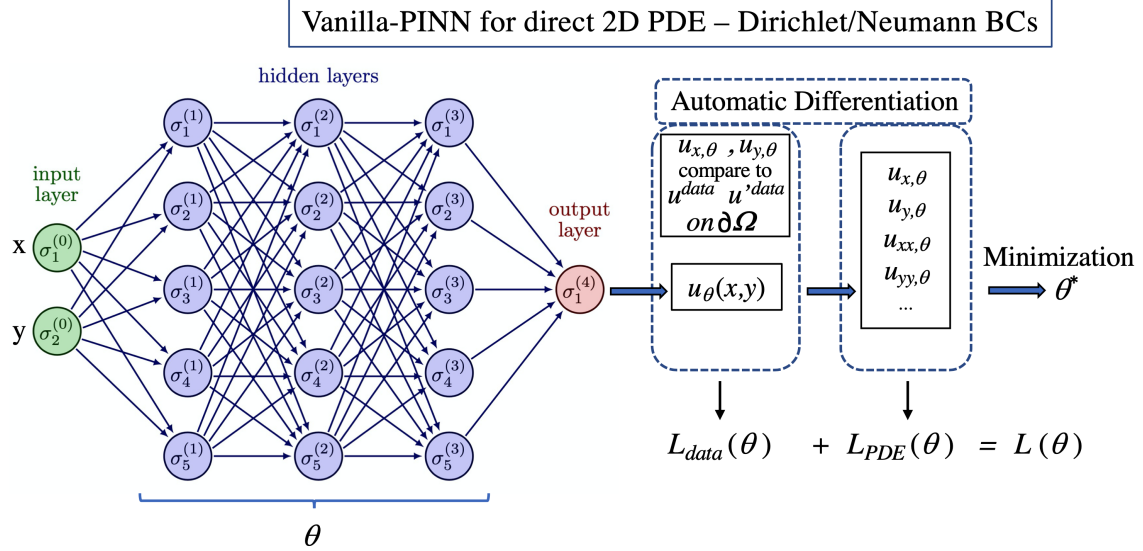


Figure 3: Schematic representation variant of previous figure where Neumann or Neumann-Dirichlet BCs are involved instead of purely Dirichlet BCs. The training data set includes additional knowledge on the exact derivatives  $u'^{data}$ .

## 2.4 PINNs for solving PDEs

In PINNs approach, a specific loss function  $L_{PDE}$  can be defined as,

$$L_{PDE}(\theta) = \frac{1}{N_c} \sum_{i=1}^{N_c} |\mathcal{F}(u_\theta(\mathbf{x}_i))|^2, \quad (10)$$

where the evaluation of the residual equation is performed on a set of  $N_c$  points denoted as  $\mathbf{x}_i$ . These points are commonly referred to as collocation points. A composite total loss function is typically formulated as follows

$$L(\theta) = \omega_{data} L_{data}(\theta) + \omega_{PDE} L_{PDE}(\theta), \quad (11)$$

where  $\omega_{data}$  and  $\omega_{PDE}$  are weights to be assigned to ameliorate potential imbalances between the two partial losses. These weights can be user-specified or automatically tuned. In this way, the previously described gradient descent algorithm given by equation (9) is applied to iteratively reduce the total loss. By including boundary data in the training dataset, the neural network can learn to approximate the solution not only within the domain but also at the boundaries where the known solutions are available. PINNs are thus well-suited for solving PDEs in inverse problems in a data-driven manner.

In the context of solving PDEs in direct and parametric problems, for cases involving purely Dirichlet BCs, the training data set is generally reduced to the sole solution value at the boundary. However, for problems involving Neumann BCs or a combination of Neumann and Dirichlet BCs (mixed Neumann-Dirichlet) the training dataset must extend beyond simple solution values. In these cases (Neumann BCs), since Neumann BCs involve the specification of perpendicular derivative values at the boundaries, the training dataset needs to include information about these derivatives.

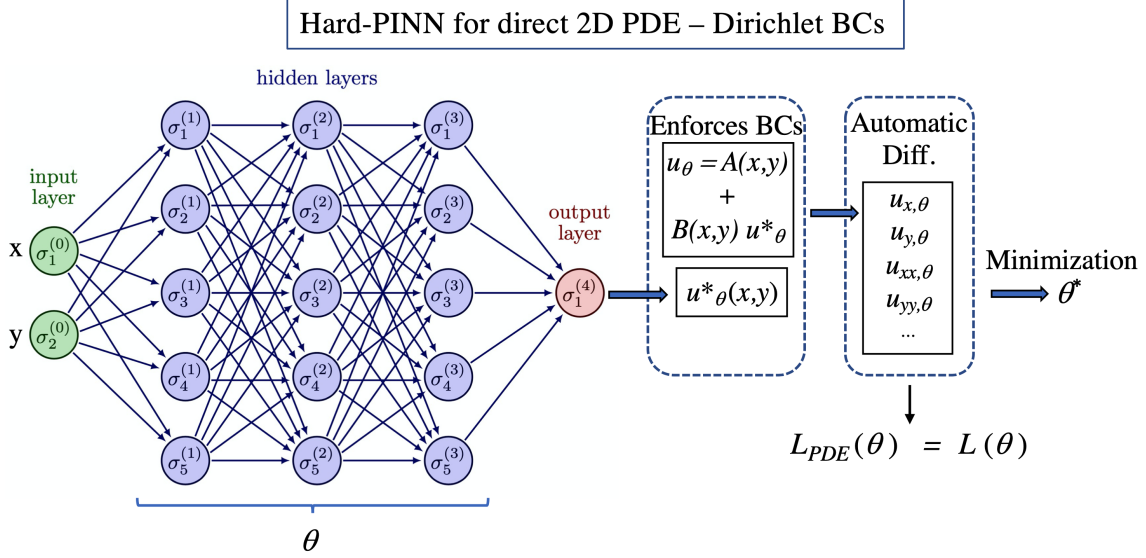


Figure 4: Schematic representation of a hard constraints BCs problem corresponding to previous figure (see text). The boundary constraints are enforced via trial function.

This ensures that the neural network learns to capture the behavior of the solution with respect to the normal derivative at the boundary. In other cases (Mixed Neumann-Dirichlet BCs), the training dataset should incorporate solution values at Dirichlet boundaries and also derivative information at Neumann boundaries.

A schematic representation of the architecture of a neural network designed to solve a PDE using PINNs is visible in Fig. 2. For simplicity, the weights are taken to be unity in this example. This scheme corresponds to a direct problem involving Dirichlet BCs imposed with soft constraints, as the solution on the boundary is not exactly enforced in this way. A similar problem involving Neumann BCs or mixed Neumann-Dirichlet BCs is schematized in Fig. 3. Note that, the procedure used to impose the derivative values for Neumann BCs is slightly different from the one proposed in Baty (2023b). Indeed, in the latter work the first collocation point was used (see Eq. 5 in the manuscript), contrary to the present work where the derivative values are part of the training data set.

As explained in introduction, an alternative option to exactly enforce BCs is to employ a well-behaved trial function (Lagaris 1998),  $u_\theta(x,y) = A(x,y) + B(x,y)u_*^\theta(x,y)$ , where now  $u_*^\theta(x,y)$  is the output value resulting from the NN transformation to be distinguished from the final predicted solution  $u_\theta(x,y)$ . In this way the use of a training data set is not necessary, and only  $L_{PDE}(\theta)$  survives to form the used loss function  $L(\theta)$ . The latter variant using thus hard boundary constraints is schematized in Fig. 4.

For a 1D spatial (i.e.  $x$ ) parametric problem,  $y$  must be replaced by  $\mu$ , and the problem is thus similar to the 2D spatial problems schematized in Figs 2-4.

Finally, for a 1D inverse problem, only one input neuron is needed for the space coordinate ( $x$ ), and the unknown parameter  $\mu$  is learned exactly as an additional network parameter like the weights and biases  $\theta$  (see further in the paper), as can be seen in the schematic representation of Fig. 5.

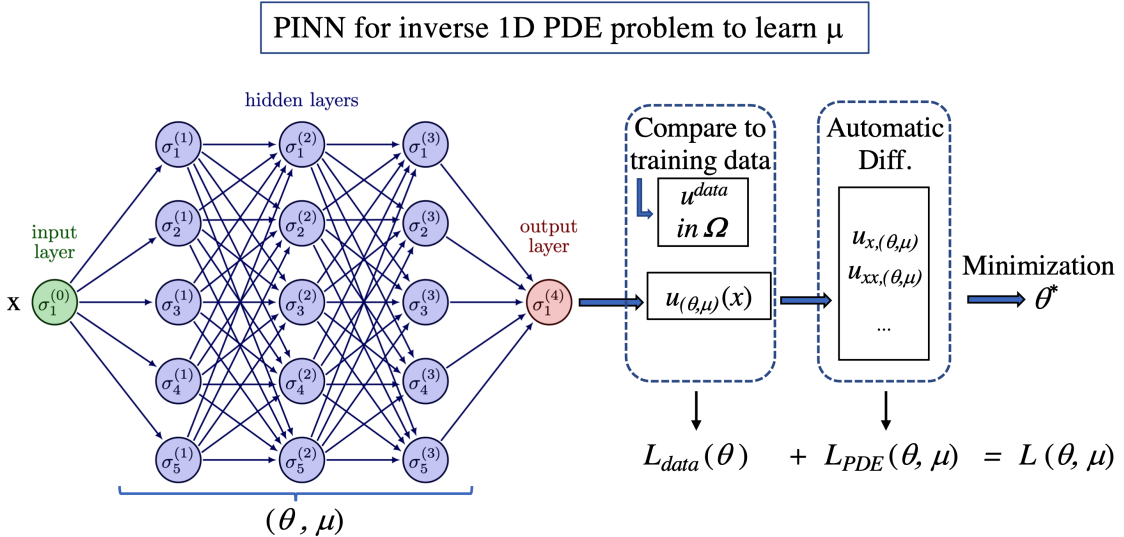


Figure 5: Schematic representation of an inverse problem. A 1D differential equation is considered (ODE in fact) parametrized with an unknown coefficient  $\mu$  to be discovered. The training data set must include data from the whole domain  $\Omega$  (not only at boundaries).

## 2.5 Python codes

The TensorFlow/Pytorch Python-based codes and data-sets accompanying this manuscript are available on the GitHub repository<sup>1</sup>. We have chosen to use very simple deep feed-forward networks architectures with hyperbolic activation functions. In this work, the tuning of the architecture of the network (number of hidden layers, number of neurons per layer) and of the other hyper-parameters (learning rate, loss weights) is done manually. Although more systematic/automatic procedures could be used, this is a difficult task not considered in this work. Note that, for the examples considered in this work, the number of employed hidden layers can typically vary between 4 and 7 and the number neurons per layer between 20 and 40. The chosen learning rate is also taken in the range varying between  $10^{-4}$  and  $10^{-3}$ , as a too small value leads to a very slow convergence and a too high value to convergence difficulties due to strong oscillations in the gradient descent algorithm. The choice of the exact optimizer variant is also important, and the best (and simpler) option is generally provided by the Adam optimizer.

## 3 Laplace equation

In order to illustrate a first practical implementation of the method, we consider a simple Laplace equation in 2D cartesian coordinates:

$$u_{xx} + u_{yy} = 0, \quad (12)$$

with  $u_{xx}$  and  $u_{yy}$  being the second order derivatives of  $u$  with respect to  $x$  and  $y$  respectively. The integration domain is a square with  $\Omega = [-1, 1] \times [-1, 1]$ . We also focus on a case having the exact

---

<sup>1</sup><https://github.com/hubertbaty/PINNS-PDE>

solution  $u(x, y) = x^2 - y^2$ . Of course, the Dirichlet BCs must match the correct exact solution values.

For Laplace equation, I propose to use the two variants of PINNs technique on a Dirichlet BCs problem, namely the vanilla-PINNs and hard-PINNs, and comparing their results.

### 3.1 Using vanilla-PINNs on Dirichlet BCs problem

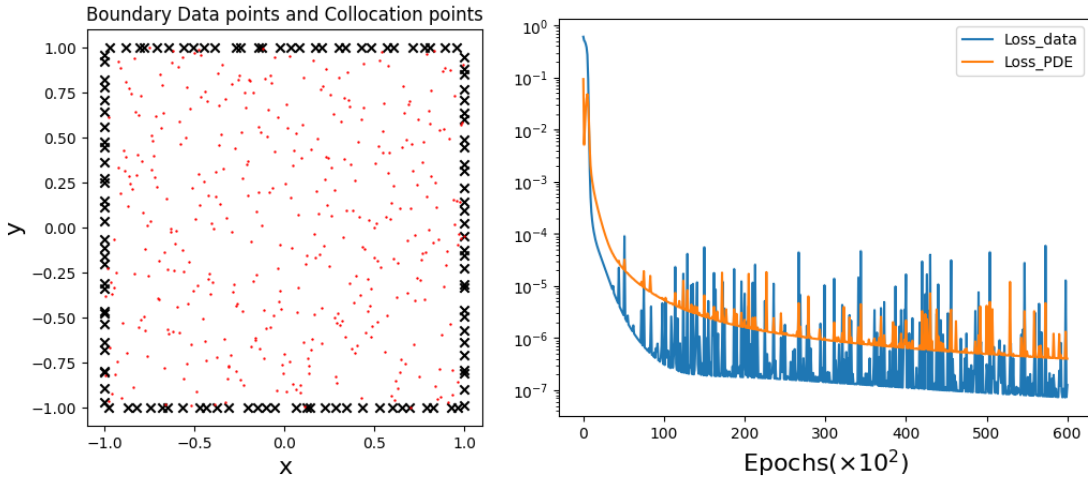


Figure 6: (Left panel) Distribution of data sets showing the space localization of training data points at the four boundaries (i.e.  $N_{data} = 120$ ) and collocation points (i.e.  $N_c = 400$ ) inside the domain, for solving Laplace problem using vanilla-PINNs. (Right panel) Evolution of the two partial losses  $L_{data}$  and  $L_{PDE}$  as functions of the number of iterations (i.e. epochs).

First, we need to generate a data set of training data with points localized at the 4 boundaries, i.e.  $x \pm 1$  and  $y \pm 1$ . In this example we choose 120 points (30 per boundary) with a randomly distribution. We also need to generate the set of collocation points inside the domain, e.g. 400 randomly distributed points are used. Note that, I use a pseudo-random distribution (Latin-hypercube strategy) in order to avoid empty regions. The resulting data generation is illustrated in Fig. 6 (left panel).

We apply the PINN algorithm schematized in Fig. 2. The evolution of the two loss functions with the training epochs that are reported in Fig. 6 (right panel), shows the convergence toward the predicted solution, as very small values are obtained at the end. Note that the training is stopped after 60000 epochs. For this problem, I have chosen a network architecture having 5 hidden layers with 20 neurons per layer. This represents 1761 learned parameters. A learning rate of  $l_r = 2 \times 10^{-4}$  is also chosen. The latter parameters choice slightly influences the results but is not fundamental as long as the number of layers/neurons is not too small (Baty 2023a). A faster convergence can be also obtained by taking a variable learning rate with a decreasing value with the advance of the training process.

The solution and the error distribution at the end of the training are plotted in Fig. 7 exhibiting a maximum absolute error of order 0.0008, This is well confirmed by inspecting corresponding one dimensional cuts comparing predicted and exact solutions, as can be seen in Fig. 8. Note that the predicted PINNs solution and associated error distribution are obtained using a third set of points

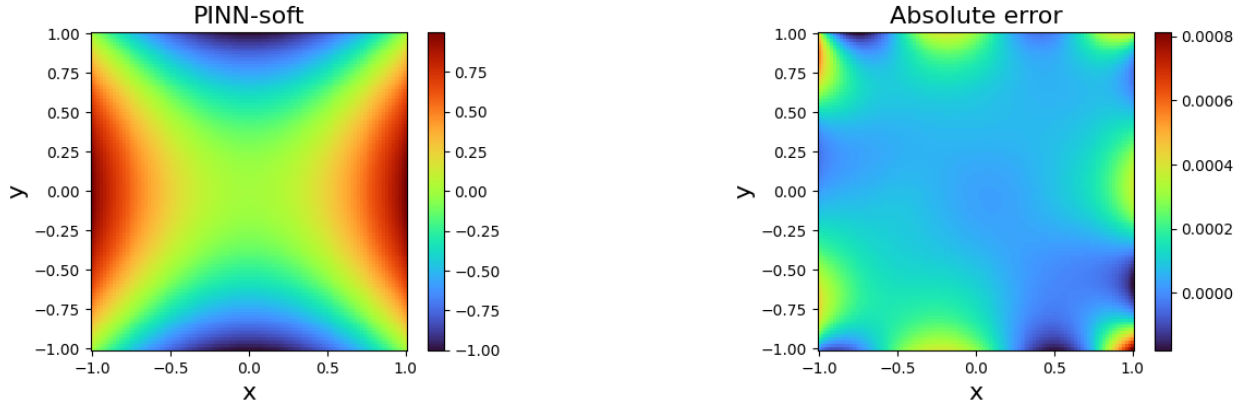


Figure 7: Solution (left panel) and absolute error (right panel) distributions as colored iso-contours corresponding to problem associated to the previous figure.

(different from the collocation points) that is taken to be a uniform grid of  $100 \times 100$  points here, otherwise the error could be artificially small (overfitting effect). One must also note that the error is higher near the boundary due to the coexistence of data/collocation points in these regions. In this way, once trained, the network allows to predict the solution quasi-instantaneously at any point inside the integration domain, without the need for interpolation (as done e.g. with finite-difference methods when the point is situated between two grid points). The precision of PINNs is known to be very good but less than more traditional methods (e.g. like in finite-element codes). This is a general property of minimization techniques based on gradient descent algorithms (Press et al. 2007; Baty 2023). However, a finer tuning of the network parameters together with the introduction of optimal combinations for weights of the partial losses can generally ameliorate the results, which is beyond the scope of this work.

Traditional numerical schemes are generally characterized by some convergence order due to the space discretization. For example, a method of order two means that the associated truncation error is divided by 4 when the space discretization factor is divided by 2, resulting in a precise given decreasing parabolic scaling law. PINNs are statistical methods that are consequently not expected to follow such law. More precisely, multiplying by 2 (for example) the number of collocation points and/or the number of training data points does not necessarily lead to a dependence law for the error. The only well established result is that, there is a minimum number of points (depending on the problem) necessary for convergence towards an acceptable solution. There is also a minimum number of hidden layers and number of neurons per layer. A too large architecture can even degrade the precision of the results. One can refer to tests done on Lane-Emden ODEs on the latter property (Baty 2023a, Baty 2023b).

### 3.2 Using hard-PINNs on Dirichlet BCs problems

We consider the same problem as in the previous sub-section, but following instead the variant schematized in Fig. 4. Only the collocation data set is necessary, and generated in the same way as previously using vanilla-PINNs. However, the predicted solution  $u_\theta$  now differs from the function  $u_\theta^*$  resulting from the output neural network transformation. Indeed, following Lagaris (1998), the

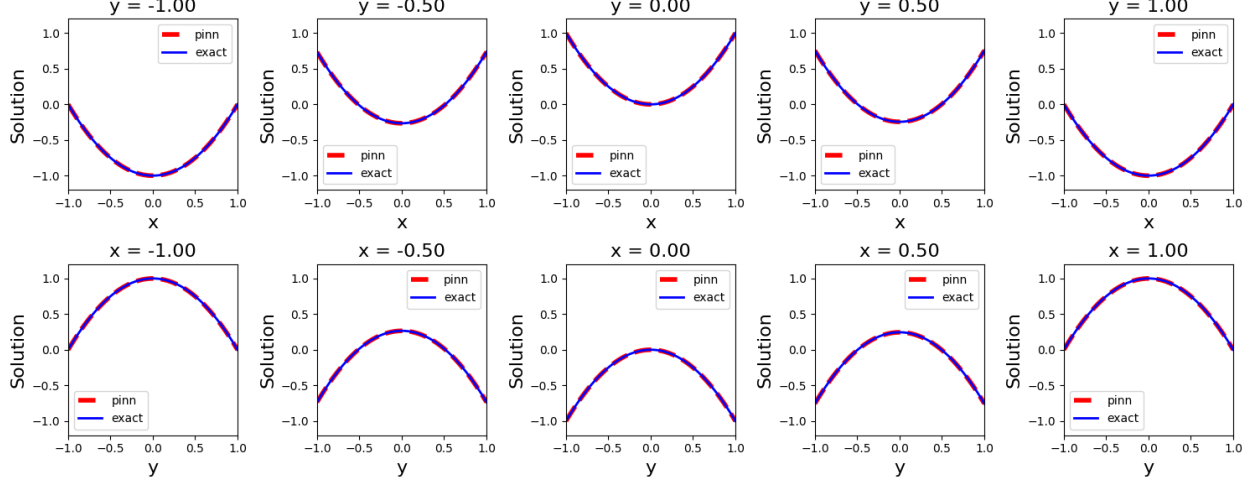


Figure 8: One-dimensional solution obtained for different  $x$  and  $y$  particular values compared with the exact analytical solution (plain line) corresponding to the previous figure.

predicted solution  $u_\theta$  can be written as,

$$u_\theta = A(x, y) + B(x, y)u_\theta^*, \quad (13)$$

where the function  $A(x, y)$  is designed to exactly satisfy the BCs without any adjustable parameter, and the remaining form  $B(x, y)u_\theta^*$  is constructed so as to not contribute to the BCs. The adjustable parameters are thus contained in the neural network output function only that is now  $u_\theta^*$ , and the function  $B(x, y)$  must vanish at the boundaries. The choice of the two functions  $A$  and  $B$  is not unique and can affect the efficiency of the algorithm.

In the present example, following prescriptions given by Lagaris (1998), we have  $B = (1-x)(1+x)(1-y)(1+y)$  and  $A = (1-y^2) + (x^2 - 1)$ . This is  $u_\theta$  that is used to evaluate the loss function  $L(\theta) = L_{PDE}(\theta)$  in the minimization procedure, as it should satisfy the PDE contrary to  $u_\theta^*$ . The loss function is based on the residual that is simply  $\mathcal{F} = u_{xx} + u_{yy}$ . Note that, it is not always simple (or even possible) to define the two functions  $A$  and  $B$ , especially when the boundaries are more complex or/and the BCs involve Neumann conditions (see Lagaris 1998).

Following the PINN algorithm schematized in Fig. 4, we can thus solve the same previous Laplace equation. The results are plotted in Fig. 9 and Fig. 10. Note that only collocation points are now necessary. The precision is better compared to results obtained using vanilla-PINNs, as the maximum absolute error is now of order  $5 \times 10^{-5}$ . Moreover, the error is mainly localized inside the domain. This was expected as the boundary values are exactly imposed with this variant. However, as explained in the previous figure, this is not always easy/possible to use this method, contrary to the vanilla-PINN variant.

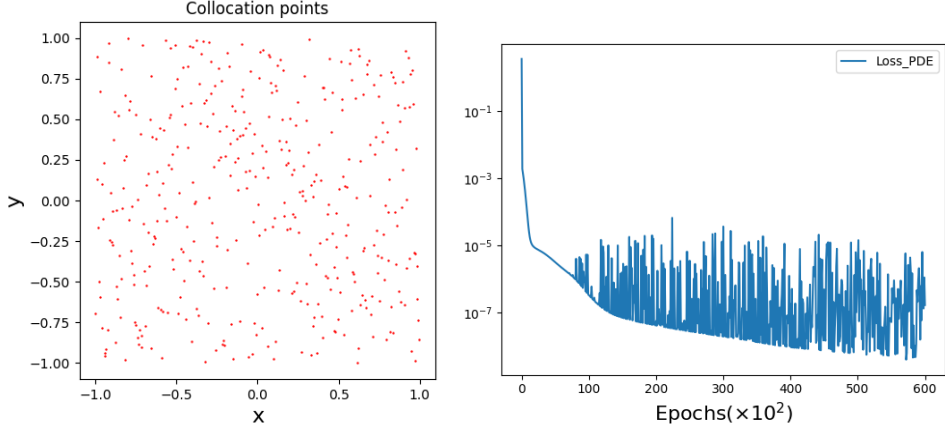


Figure 9: (Left panel) Distribution of data sets showing collocation points (i.e.  $N_c = 400$ ) inside the domain, for solving Laplace problem using hard-PINNs. (Right panel) Evolution of the total loss  $L = L_{PDE}$  as function of the number of iterations (i.e. epochs).

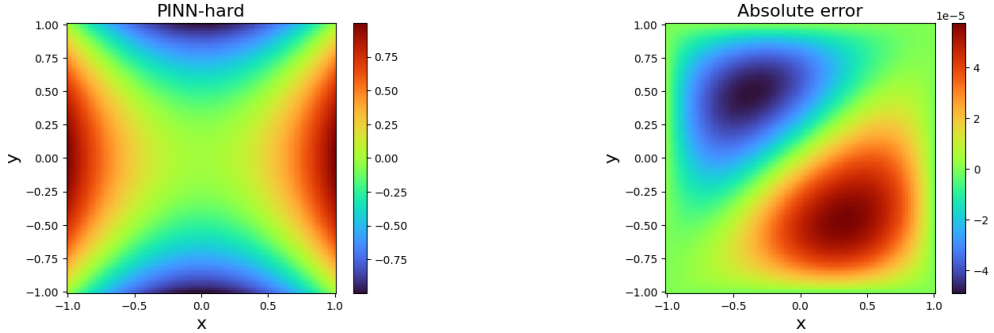


Figure 10: Solution (left panel) and absolute error (right panel) distributions as colored iso-contours corresponding to problem associated to the previous figure.

## 4 Poisson equations

In this section, we test the method on Poisson-type equations in 2D cartesian coordinates. Thus, we consider the following form,

$$u_{xx} + u_{yy} = f(x, y), \quad (14)$$

having the following 5 manufactured exact solutions taken from Nishikawa (2023):

$$\begin{aligned} (a) \quad & u(x, y) = e^{xy} \\ (b) \quad & u(x, y) = e^{kx} \sin(ky) + \frac{1}{4}(x^2 + y^2) \\ (c) \quad & u(x, y) = \sinh(x) \\ (d) \quad & u(x, y) = e^{x^2+y^2} \\ (e) \quad & u(x, y) = e^{xy} + \sinh(x) \end{aligned} \quad (15)$$

for respectively,

$$\begin{aligned}
(a) \quad & f(x, y) = e^{xy}(x^2 + y^2) \\
(b) \quad & f(x, y) = 1 \\
(c) \quad & f(x, y) = \sinh(x) \\
(d) \quad & f(x, y) = 4(x^2 + y^2 + 1)e^{x^2+y^2} \\
(e) \quad & f(x, y) = e^{xy}(x^2 + y^2) + \sinh(x)
\end{aligned} \tag{16}$$

We consider the integration domain  $\Omega = [0, 1] \times [0, 1]$  with different types of boundary conditions specified below.

In this section, I propose to compare the use of different BCs with vanilla-PINNs variant (only) on Poisson problems. Now, the loss function for PDE is based on the residual equation  $\mathcal{F} = u_{xx} + u_{yy} - f(x, y)$ .

#### 4.1 Using vanilla-PINNs on Dirichlet problems

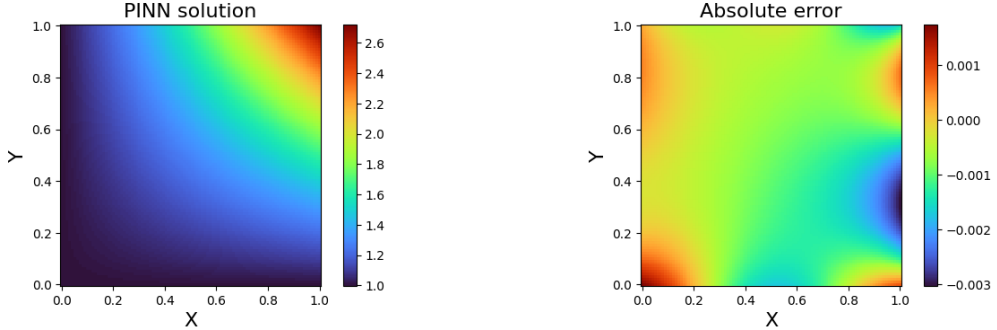


Figure 11: Vanilla-PINNs solution (left panel) and associated absolute error (right panel) distributions as colored iso-contours corresponding to Poisson-problem (case-a) equation with Dirichlet BCs.

First, we need to generate a data set of training data with points localized at the 4 boundaries, i.e.  $x = 0$ ,  $x = 1$ ,  $y = 0$ , and  $y = 1$ . As illustrated for Poisson problem, we choose 120 points (30 per boundary) with a randomly distribution. We also need to generate the set of collocation points inside the domain, e.g. 400 randomly distributed points (with Latin-hypercube strategy) are used.

We apply the PINN algorithm schematized in Fig. 2, to solve the equation for the first case (a). The evolution of the two loss functions with the training epochs that are reported in Fig. 11, shows the convergence toward the predicted solution, as very small values are obtained at the end. Note that the training is stopped after 60000 epochs. For such Poisson PDE the PDE loss function is taken to be based on  $\mathcal{F} = u_{xx} + u_{yy} - f(x, y)$ . For this problem, I have chosen a network architecture having 6 hidden layers with 20 neurons per layer. This represents 2181 learned parameters. A learning rate of  $l_r = 3 \times 10^{-4}$  is also chosen.

The solution and the error distribution at the end of the training are plotted in Fig. 12 exhibiting a maximum absolute error of order 0.003 (the corresponding maximum relative error is similar to the previous Poisson problem). Similar results are obtain for the other equations, as one can see on results reported in appendix.

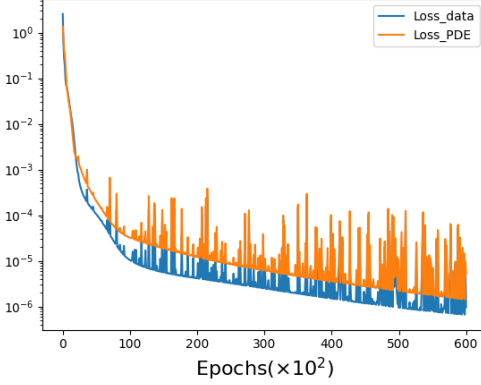


Figure 12: Evolution of the two partial losses  $L_{data}$  and  $L_{PDE}$  as functions of the number of iterations (i.e. epochs) for Poisson equation (case-a) with Dirichlet BCs using vanilla-PINN, associated to previous figure.

Of course, if the BCs are applied only on a part of the whole boundary  $\partial\Omega$  (for example on 3 or even on 2 of the four boundaries), the solution can be also obtained but with a lower accuracy.

## 4.2 Using vanilla-PINNs on Neumann problems

Now, we solve the same Poisson equation using Neumann BCs at the 4 boundaries. The results show a convergence towards a wrong solution that is the expected exact solution up to an additive constant (the latter value being 3.47 for case-a, see Figs. 13-14).

This is not surprising as the solution to Poisson problem subject to pure Neumann conditions is known to be unique only up to an overall additive constant. One can check this is also the case solution to other Poisson equations (cases b-e), as plotted in Appendix.

This example illustrates that, the convergence of the loss function towards a low value does not guarantee obtaining the exact solution.

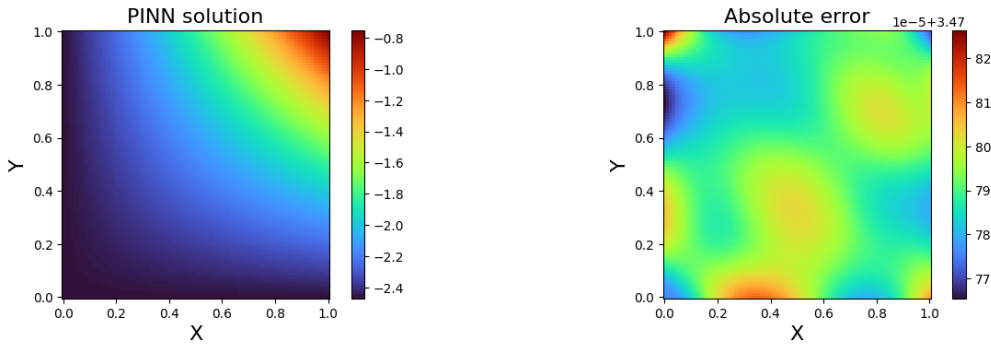


Figure 13: Solution (left panel) and absolute error (right panel) distributions as colored iso-contours corresponding to the Poisson problem (case-a) with Neumann BCs and vanilla-PINN.

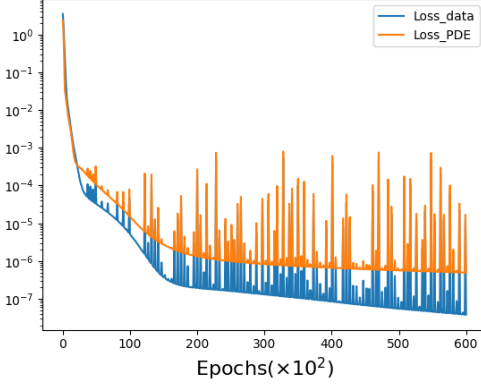


Figure 14: Evolution of the two partial losses  $L_{data}$  and  $L_{PDE}$  as functions of the number of iterations (i.e. epochs) for Poisson equation (case a) with Neumann BCs using vanilla-PINN.

### 4.3 Using vanilla-PINNs on Neumann-Dirichlet problems

Using mixed boundary conditions (i.e. Dirichlet on part on boundary  $\partial\Omega$  and Neumann on the rest) lead to the exact solution as for purely Dirichlet BCs. An example of results obtained for the first Poisson equation (a-case), where Dirichlet BC values are imposed at  $x = 1$  and  $y = 1$  and Neumann BC values at the 2 other boundaries ( $x = 0$  and  $y = 0$ ), is illustrated in Fig. 15.

Although it depends on cases considered, the error value is similar with (generally) a slightly better accuracy when compared to results for purely Dirichlet BCs.

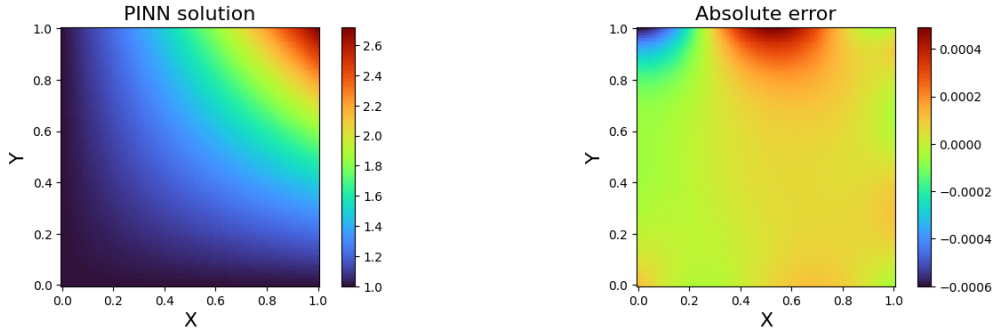


Figure 15: Solution (left panel) and absolute error (right panel) distributions as colored iso-contours corresponding to the Poisson problem (case a) with mixed Dirichlet-Neumann BCs and vanilla-PINN (see text).

### 4.4 Using vanilla-PINNs on Cauchy problems

We consider Cauchy boundary conditions (where both the solution and the perpendicular derivative are simultaneously specified on the same boundary). For example, for the results obtained in Fig. 16 on the case (a), we have imposed the exact solutions and perpendicular derivatives at the two boundaries  $x = 0$  and  $x = 1$  only. The accuracy appears to be similar to solution obtained for the same problem using mixed boundary conditions (see previous sub-section).

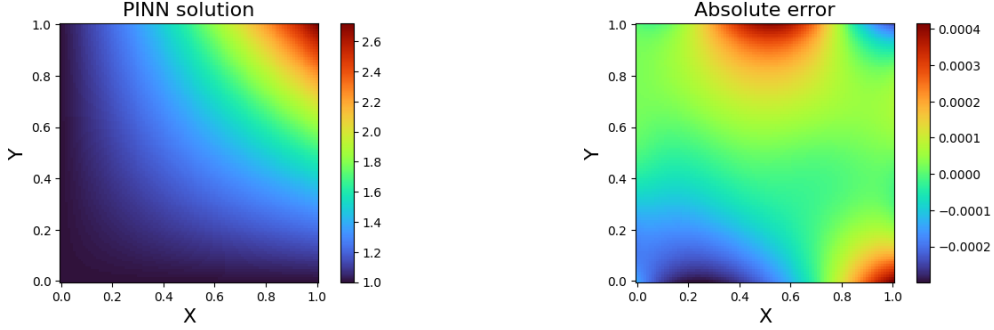


Figure 16: Solution (left panel) and absolute error (right panel) distributions as colored iso-contours corresponding to the Poisson problem (case a) with Cauchy BCs and vanilla-PINN (see text).

## 5 Helmholtz equations

### 5.1 Specific problem related to astrophysics

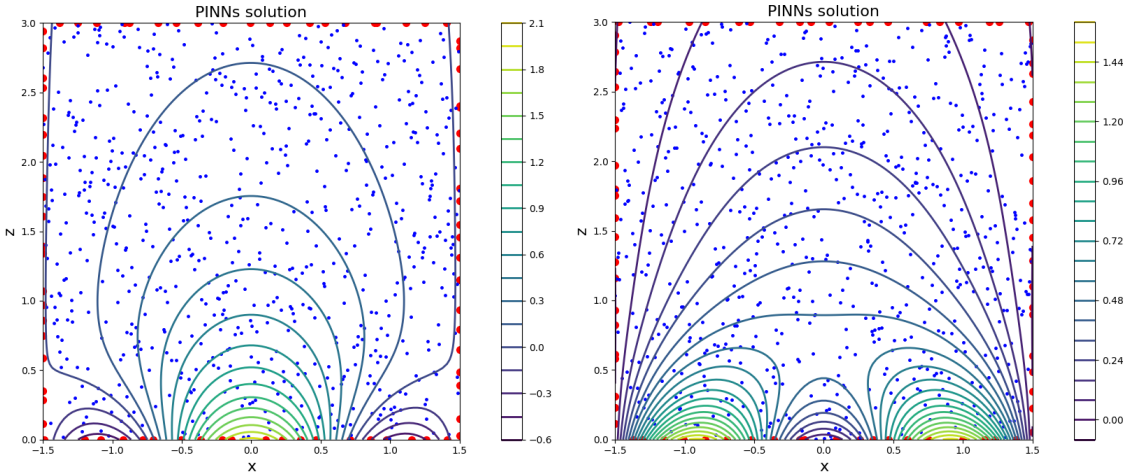


Figure 17: Solutions (iso-contours of  $u(x, z)$ ) predicted by PINNs solver for the Helmholtz equation for two cases, i.e. for the parameters combination  $(a_1, a_2, a_3)$  equal to  $(1, 0, 1)$  and  $(1, 0, -1)$  in left and right panel respectively. The distribution of data sets (training and collocation points) is also indicated using red and blue dots at the boundary and inside the domain respectively.

Following a previous work (Baty & Vignon 2024), we solve an Helmholtz equation,

$$\Delta u + c^2 u = 0, \quad (17)$$

where  $c$  is a constant and  $\Delta = \frac{\partial^2}{\partial x^2} + \frac{\partial^2}{\partial z^2}$  is the cartesian Laplacian operator. The spatial integration domain with  $(x, z)$  extending between  $[-\frac{L}{2}, \frac{L}{2}]$  respectively is taken.

In an astrophysical context, this equation represents an equilibrium magnetic structure. This is for example the case of magnetic arcades observed in the solar corona. The scalar function  $u(x, z)$  is known as a flux function allowing to deduce the magnetic field vector component in the  $(x, z)$

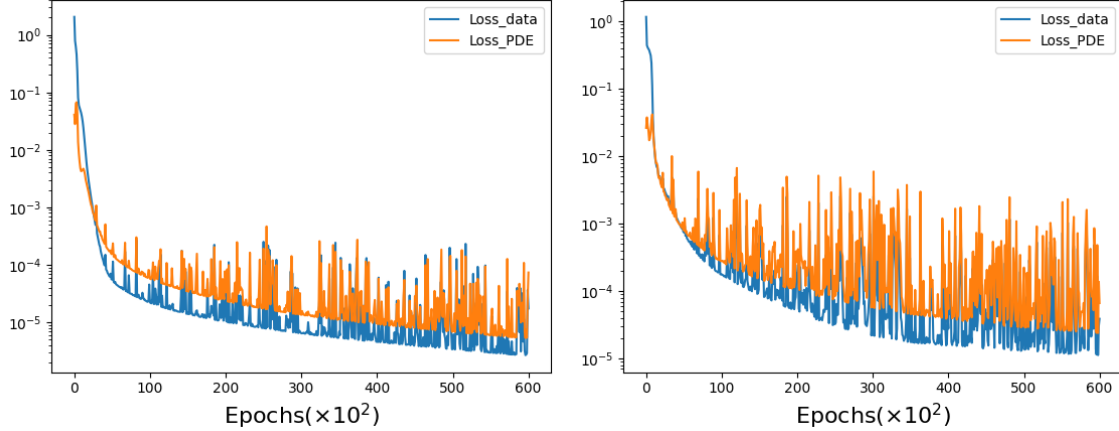


Figure 18: Evolution of the losses (training data and PDE) during the training as functions of epochs, corresponding to the two cases respectively (see previous figure).

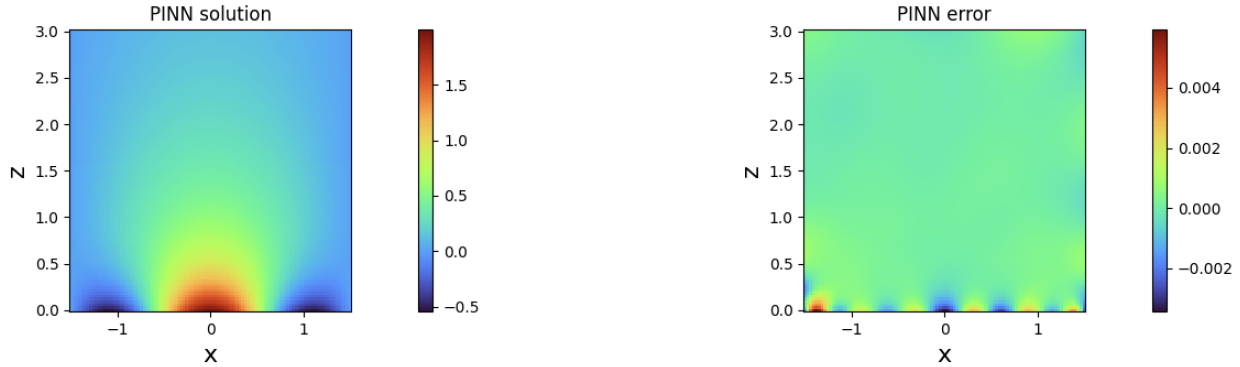


Figure 19: Predicted solution (left panel) and absolute error distribution (right panel) using colored iso-contours, corresponding to the first case parameters combination  $(a_1, a_2, a_3)$  equal to  $(1, 0, 1)$  of the Helmholtz problem (see text and the two previous figures).

plane and magnetic field lines, via isocontour values of  $u$ . The sun surface is situated at  $z = 0$  as  $z$  represents the altitude. The remaining magnetic field component  $B_y$  being simply added to the previous one in case of translational symmetry generally assumed in this invariant direction. On other words, the total magnetic field may be written as,

$$\mathbf{B}(x, z) = \nabla u(x, z) \times \mathbf{e}_y + B_y(u) \mathbf{e}_y, \quad (18)$$

where  $\mathbf{e}_y$  is the unit vector of the cartesian basis along the  $y$  direction. Exact solutions for triple arcade structures can be obtained using Fourier-series as

$$u(x, z) = \sum_{k=1}^3 \exp(-\nu z) \left[ a_k \cos \left( \frac{k\pi}{L} x \right) \right]. \quad (19)$$

The latter solution is periodic in  $x$ , and the relationship  $\nu^2 = \frac{k^2\pi^2}{L^2} - c^2$  applies as a consequence

of the above Helmholtz equation. More details about the context can be found in Baty & Vigon (2024) and references therein.

## 5.2 Solutions using vanilla-PINNs with Dirichlet BCs

We illustrate the use of our PINN-solver on two cases, i.e. for the two combinations of  $(a_1, a_2, a_3)$  parameters that are  $(1, 0, 1)$  and  $(1, 0, -1)$ . The other physical parameters are  $L = 3$  and  $c = 0.8$ .

We have chosen 30 training data points per boundary layer (i.e.  $N_{data} = 120$ ) with a random distribution, as one can see in Fig. 17 (with red dots on the boundaries) where the predicted solution are plotted for the two cases. The exact solution is used to prescribe the training data values as done for the previous equations. For the collocation data set,  $N_{data} = 700$  points are generated inside the integration domain using a pseudo-random distribution (i.e. latin-hypercube strategy) as one can see with blue dots. The evolution of the loss functions with the training epochs that is reported in Fig. 18 for the first case, illustrates the convergence toward the predicted solution. Note that the training is stopped after 60000 epochs. We have chosen a network architecture having 7 hidden layers with 20 neurons per layer (i.e. corresponding number of 2601 learning parameters for the neural network), and a fixed learning rate of  $l_r = 3 \times 10^{-4}$ . For such Helmholtz PDE, the PDE loss function is taken to be  $\mathcal{F} = u_{xx} + u_{zz} + c^2 u$ .

The error distribution at the end of the training for the first case is plotted in Fig. 19 exhibiting a maximum absolute error of order 0.004, which also corresponds to a similar maximum relative error of order 0.002 (the maximum magnitude solution value being of order two). Note that, again the predicted PINNs solution and associated error distribution are obtained using a third set of points (different from the collocation points) that is taken to be a uniform grid of  $100 \times 100$  points here. In this way, once trained, the network allows to predict the solution quasi-instantaneously at any point inside the integration domain, without the need for interpolation (as done for with classical tabular solutions). One must also note that the error is higher near the boundary due to the higher gradient of the solution and to the coexistence of data/collocation points in these regions.

The precision of PINN-solver is very good but less than more traditional methods (like in finite-element codes for example). This is a general property of minimization techniques based on gradient descent algorithms (Press et al. 2007, Baty 2023a). However, a finer tuning of the network parameters together with the introduction of optimal combinations for weights of the partial losses can generally ameliorate the results.

## 5.3 More general Helmholtz problems

Let us consider the Helmholtz equation (i.e. Eq. 17) with  $c$  coefficient obeying  $c^2 = (c_x^2 + c_y^2)\pi^2$ , with  $c_x$  and  $c_y$  being integers. There may exist different  $c_x, c_y$  values for which the equation is satisfied in an approximate way. Equivalently, we may have,  $(c_x^2 + c_y^2)\pi^2 = c^2(1 \pm \epsilon) \simeq c^2$ , with  $\epsilon$  a small value parameter. In this case, a vanilla-PINNs solver is expected to not converge well or to fail to predict the exact solution.

## 6 Grad-Shafranov equations

Another equation represents a second important issue for approximating magnetic equilibria of plasma in the solar corona. The latter that is known as Gad-Shafranov (GS) equation, is used to model curved loop-like structures. It is also used to approximate the magnetohydrodynamic (MHD)

equilibria of plasma confined in toroidal magnetic devices that aim at achieving thermonuclear fusion experiments like tokamaks.

The GS equation can be written as

$$-\left[ \frac{\partial^2 \psi}{\partial R^2} + \frac{\partial^2 \psi}{\partial z^2} - \frac{1}{R} \frac{\partial \psi}{\partial R} \right] = G(R, z, \psi), \quad (20)$$

with a formulation using  $(R, \phi, z)$  cylindrical like variables. The scalar function  $\psi(R, z)$  is the desired solution allowing to deduce the poloidal magnetic field  $\mathbf{B}_p$  (component in the  $(R, z)$  plane) via

$$\mathbf{B}_p = \frac{1}{R} \nabla \psi \times \mathbf{e}_\phi + \frac{F(\psi)}{R} \mathbf{e}_\phi \quad (21)$$

in the axisymmetric approximation, where  $F(\psi) = RB_\phi$ . The toroidal magnetic field component is  $\mathbf{B}_\phi = B_\phi \mathbf{e}_\phi$  oriented along the toroidal unit vector  $\mathbf{e}_\phi$  (perpendicular to the poloidal plane). The right hand side source term  $G(R, z, \psi)$  includes a thermal pressure term and a second term involving a current density, and must be specified in order to solve the equation 20 (see below).

The elliptic differential operator (left hand side of equation ) can be rewritten, as multiplying the equation by  $R$ , leads to the following residual form

$$\mathcal{F} = \left[ R \frac{\partial^2 \psi}{\partial R^2} + R \frac{\partial^2 \psi}{\partial z^2} - \frac{\partial \psi}{\partial R} \right] + RG(R, z, \psi) = 0, \quad (22)$$

that is effectively used in our PINN solver.

## 6.1 Example of Soloviev equilibrium: the drop-like structure

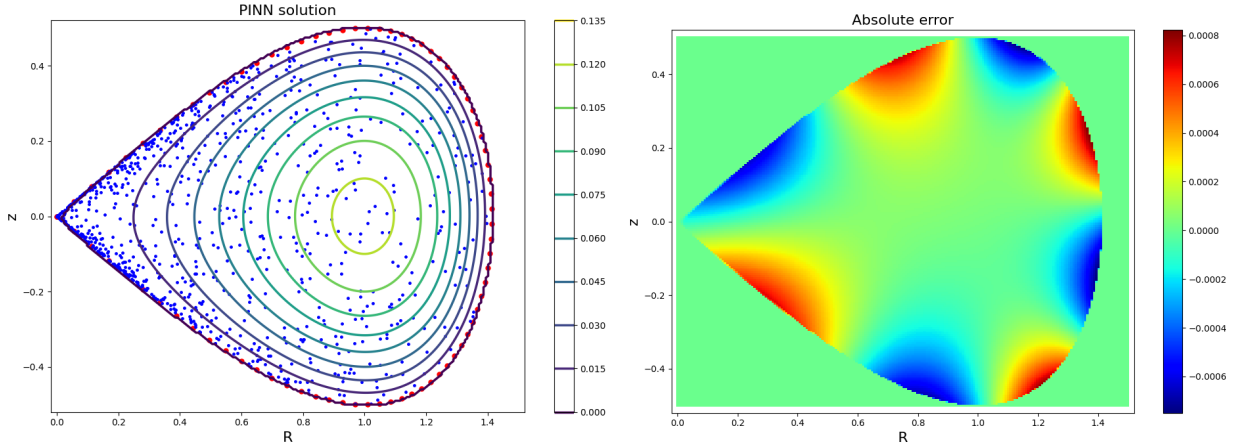


Figure 20: Predicted solution (left panel) and absolute error distribution (right panel) using colored iso-contours, for the drop-like solution of GS equation and Soloviev equilibrium. The spatial locations for training and collocation data sets used on the boundary and interior domain respectively are indicated with red and blue dots respectively.

Exact analytical solutions called Soloviev solutions are of particular importance for approximating the general solutions relevant of tokamaks and other variants of such toroidal magnetic devices

(Soloviev 1975). The latter are obtained by taking relatively simple expressions for the source term  $G(R, z)$ .

For example, assuming  $G = f_0(R^2 + R_0^2)$  leads to the exact analytical solution (see Deriaz et al. 2011)

$$\psi = \frac{f_0 R_0^2}{2} \left[ a^2 - z^2 - \frac{R^2 - R_0^2}{4R_0^2} \right], \quad (23)$$

with a simple boundary condition  $\psi = 0$  on a closed contour  $\partial\Omega$  defined by

$$\partial\Omega = \left[ R = R_0 \sqrt{1 + \frac{2a \cos(\alpha)}{R_0}}, z = aR_0, \alpha = [0 : 2\pi] \right], \quad (24)$$

where  $R_0$ ,  $a$ , and  $f_0$  are parameters to be chosen. As can be seen below, the integration domain  $\Omega$  bounded by  $\partial\Omega$  has a funny drop-like form with an  $X$ -point topology at  $z = R = 0$ , as  $\frac{\partial\psi}{\partial z} = \frac{\partial\psi}{\partial R} = 0$  at this point.

Here, we present the results obtained with our PINN solver using parameter values,  $f_0 = 1$ ,  $a = 0.5$ , and  $R_0 = 1$ . The network architecture is similar to the arcade problem where 7 hidden layers with 20 neurons per layer were chosen, which consequently represent a number of 2601 trainable parameters. We have used 80 training data points (i.e.  $N_{data} = 80$ ) with a distribution based on a uniform  $\alpha$  angle generator, and  $N_c = 870$  collocation points inside the integration domain. Contrary to the case reported in Baty & Vigon (2024), the distribution of collocation points is obtained using a pseudo-random generator with an additional concentration close to the  $X$ -point in order to get a better predicted solution there. The results are obtained after a training process with a maximum of 60000 epochs.

## 6.2 Examples of Soloviev equilibria: toroidal fusion devices

In a similar way, a PINN solver can be used to predict Soloviev-like equilibria corresponding to the parametrization  $G = A + (1 - A)R^2$  for the source term in the GS equation ( $A$  being a dimensionless parameter). The boundary of the integration domain where  $\psi$  is expected to vanish is defined in a parametric way as

$$R = 1 + \epsilon \cos(\tau + \arcsin(\delta) \sin(\tau)), \quad (25)$$

and

$$z = \epsilon \kappa \sin(\tau), \quad (26)$$

where geometric parameters  $\epsilon = a/R_0$  (inverse aspect ratio),  $\kappa$  (the elongation),  $\delta$  (the triangularity) are introduced. The remaining parameter  $\tau$  is an angle varying continuously in the range  $[0, 2\pi]$ . Note that, as described by Cerfon et al. (2011) the exact solutions are only approximately analytic. However, this parametrization presents the advantage to model Soloviev equilibria for a collection of different toroidal devices (i.e. not only tokamaks for example) as illustrated below. The geometric parameters also closely correspond to measured values from the experiments.

Using PINNs solvers similar to the previously described ones, predicted solutions corresponding to different toroidal devices easily computed. Indeed, choosing the parameters combination,  $\epsilon = 0.33$ ,  $\kappa = 1.7$ , and  $\delta = 0.32$ , together with  $A = -0.155$ , allows to model magnetic equilibria representative of the ITER tokamak configuration. A second combination with  $\epsilon = 0.78$ ,  $\kappa = 2$ , and  $\delta = 0.35$ , together with  $A = 1$ , allows to model magnetic equilibria representative of the NSTX

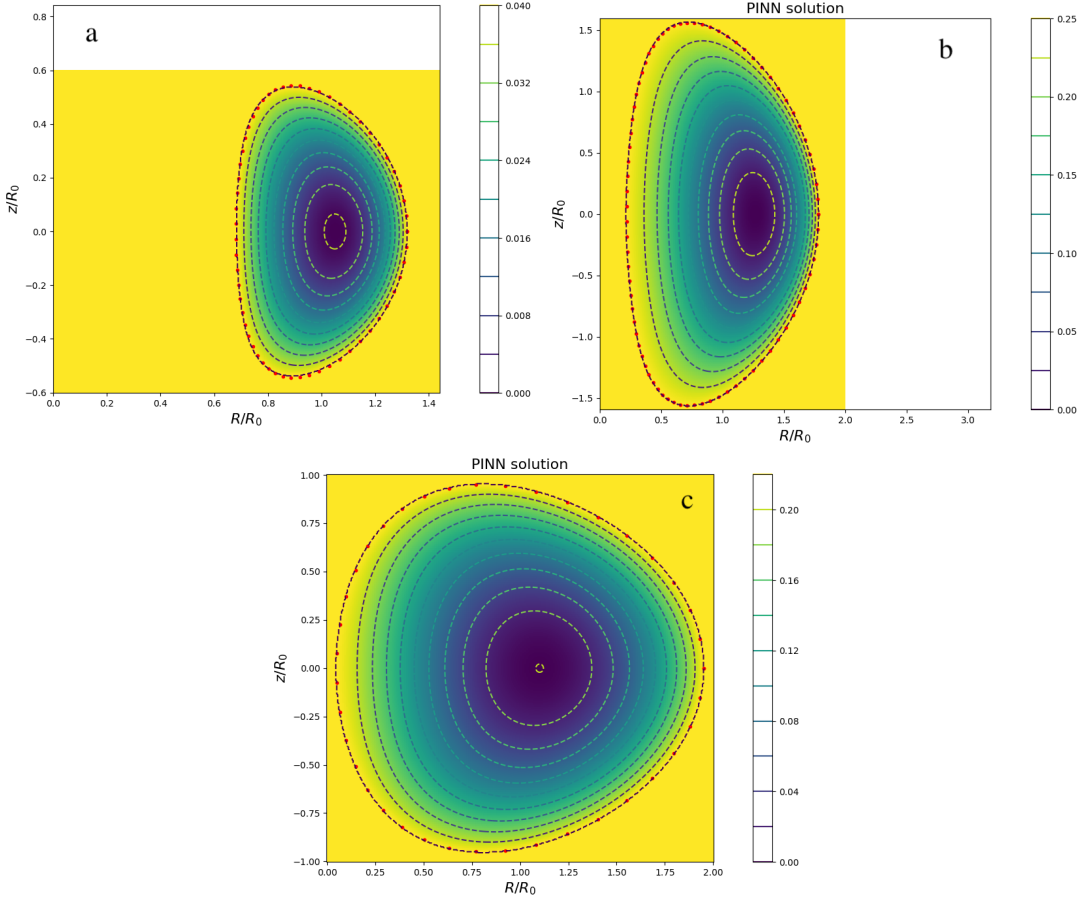


Figure 21: Predicted solutions (colored iso-contours of  $\psi$ ) for tokamak ITER-like (a panel), spherical tokamak NSTX-like (b panel), and spheromak-like (c panel) devices. Only spatial locations of training data points where  $\psi = 0$  (at the boundary) is imposed as soft (Vanilla-PINN) constraints are indicated with red dots.

spherical tokamak. And, a third combination with  $\epsilon = 0.95$ ,  $\kappa = 1$ , and  $\delta = 0.2$ , together with  $A = 1$ , allows to model magnetic equilibria representative of a spheromak. The results obtained are plotted in Fig. 21. The particular choice for these parameter values is explained in details in Cerfon et al. (2011). The choice for the neural network architecture and the numerical parameters for the gradient descent algorithm is similar to what has been done previously. Finally, note that a similar PINN solver tested on the same toroidal fusion devices have been developed by Jang et al. (2024).

### 6.3 Other examples of more general equilibria in a rectangular domain

As a simplification of the boundary, solutions of GS equilibria can be computed in a rectangular domain (see Itagaki et al. 2004), where the homogeneous solution  $\psi = 0$  is imposed. Source terms of different forms can be studied like  $G = R^l z^m$  with  $m$  and  $n$  being positive integer parameters.

A rectangular domain  $\Omega = [0.5, 1.5] \times [-0.5, 0.5]$  is taken. Note that, for this particular problems, the use of hard constraints (with Lagaris like BCs) leads to better results compared to the use of

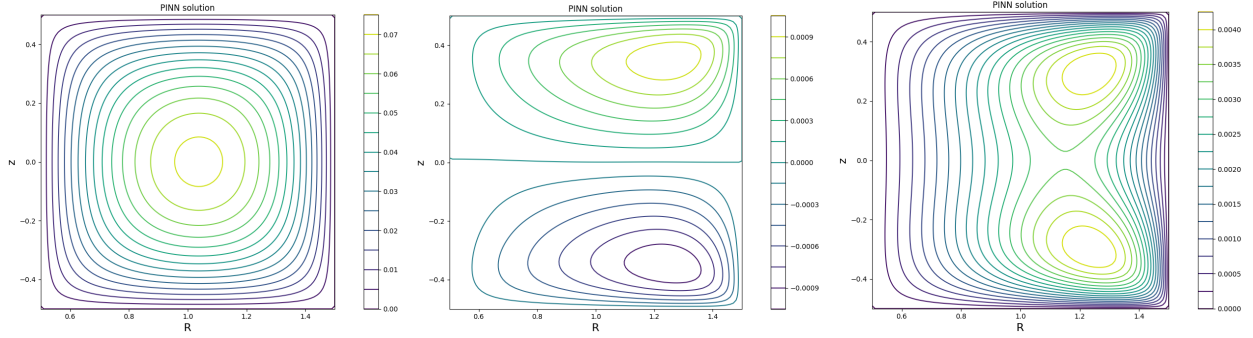


Figure 22: Predicted solutions (iso-contours of  $\psi$ ) of GS equation in a rectangular domain with three source terms,  $G = 1$ ,  $G = R^2z^3$ , and  $G = R^3z^2$  in left, middle, and right panel respectively. Hard constraints are used to impose Dirichlet BCs.

vanilla-PINNs. Indeed, following the specification proposed by Lagaris (1998) and as expressed in subsection 3.2, it is preferable to write

$$\psi_\theta = (R - 0.5)(R - 1.5)(z - 0.5)(z + 0.5)\psi_\theta^*, \quad (27)$$

where  $\psi_\theta^*$  is the output of the neural network. In this way, the predicted solution  $\psi_\theta$  automatically vanishes at the boundary and the training data set is not needed. Using PINNs solvers similar to the previously described ones, predicted solutions for three different source terms are plotted in Fig. 22.

In order to show that PINN solver can also be used for non linear source terms  $G$ , we consider a case taken from Peng et al. (2020) with  $G = 2R^2\psi[c_2(1 - \exp(-\psi^2/\sigma^2)) + 1/\sigma^2(c_1 + c_2\psi^2)\exp(-\psi^2/\sigma^2)]$  with  $\sigma^2 = 0.005$ ,  $c_1 = 0.8$ , and  $c_2 = 0.2$  in a domain  $\Omega = [0.1, 1.6] \times [-0.75, 0.75]$ . The results obtained with a PINNs solver using hard constraints are plotted in Fig. 3. In this case, the imposed Dirichlet condition value used is now  $\psi = 0.25$ . Consequently, we also use

$$\psi_\theta = (R - 0.1)(R - 1.6)(z - 0.75)(z + 0.75)\psi_\theta^*, \quad (28)$$

As there is no exact solution available, this is not possible to evaluate the error. However, our solution compares well with the solution computed in Peng et al. (2020).

## 7 Lane-Emden equations

The Lane-Emden (LE) equations are widely employed in astrophysics and relativistic mechanics. Before focusing on a precise case taken from astrophysics, it is instructive to introduce a more general mathematical form.

### 7.1 A mathematical example

Following previous papers (Bencheikh 2023 and references therein), we can consider the following two-dimensional differential form:

$$u_{xx} + \frac{\alpha}{x}u_x + u_{yy} + \frac{\beta}{y}u_y + f(u, x, y) = 0, \quad (29)$$

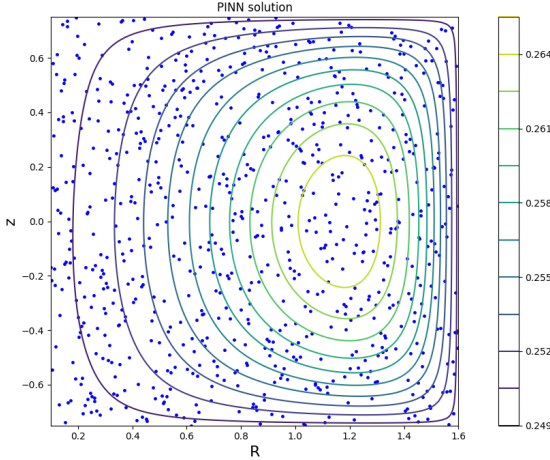


Figure 23: Predicted solutions (iso-contours of  $\psi$ ) of GS equation in a rectangular domain with a non linear source term  $G$  (see text). The location of collocation points are indicated with blue dots. There is no training data points as hard constraints (Lagaris method) are used to impose Dirichlet BCs.

where second order derivatives ( $u_{xx}$  and  $u_{yy}$ ), and first order derivatives ( $u_x$  and  $u_y$ ) of the desired solution are involved. The two scalars  $\alpha$  and  $\beta$  are real shape parameters,  $f(x, y)$  is a given scalar source function, and integration is done on a cartesian  $(x, y)$  domain.

The particularity of Lane-Emden equation lies in the singularities at  $x = 0$  and  $y = 0$ , which must be overcome by numerical integration method. As can be seen below, solvers based on PINNs algorithm are excellent choice as classical discretization is not needed. We also focus on the search for solutions in a rectangular domain with Cauchy-like conditions imposed at one or two of the four boundaries. The conditions at the other boundaries are assumed free or of Neumann type. Indeed, such problems are representative of physical examples in astrophysical context (see second subsection in this section).

As an example, we take a case with  $\alpha = \beta = 2$ , and  $f = -6(2 + x^2 + y^2)$ . The integration domain is  $\Omega = [0, 2] \times [-1, 1]$ . The exact solution can be checked to be  $u = (1 + x^2)(1 + y^2)$ . The residual form used to evaluate the PDE loss function is taken to be

$$\mathcal{F} = xyu_{xx} + \alpha yu_x + xyu_{yy} + \beta xu_y + xyf(u, x, y) = 0, \quad (30)$$

Using a PINNs solver similar to previously described ones, we can predict the solution for three distinct problems involving Cauchy-type condition at (at least) one boundary. Indeed, when we imposed Cauchy condition (i.e. using the exact solution and also the its perpendicular derivative) at the two boundaries  $x = 0$  and  $x = 1$ , the predicted PINN solution (plotted in Fig. 24) shows a rather good agreement with the exact solution inside the domain, as the maximum absolute error is 0.004. However, when the Cauchy condition is imposed only at one boundary, i.e. at  $x = 2$ , the accuracy is significantly deteriorated compared to the previous case (see Fig. 25 exhibiting a maximum absolute error of 0.30). This error is obviously mainly localized at the opposite boundary. In astrophysical context, the prescription of the perpendicular derivative at the two other boundaries (i.e. at  $y \pm 1$  can be a reasonable hypothesis. Consequently, when we impose Cauchy condition at  $x = 2$  in addition to Neumann conditions at  $y \pm 1$ , one can see that the predicted PINN solution

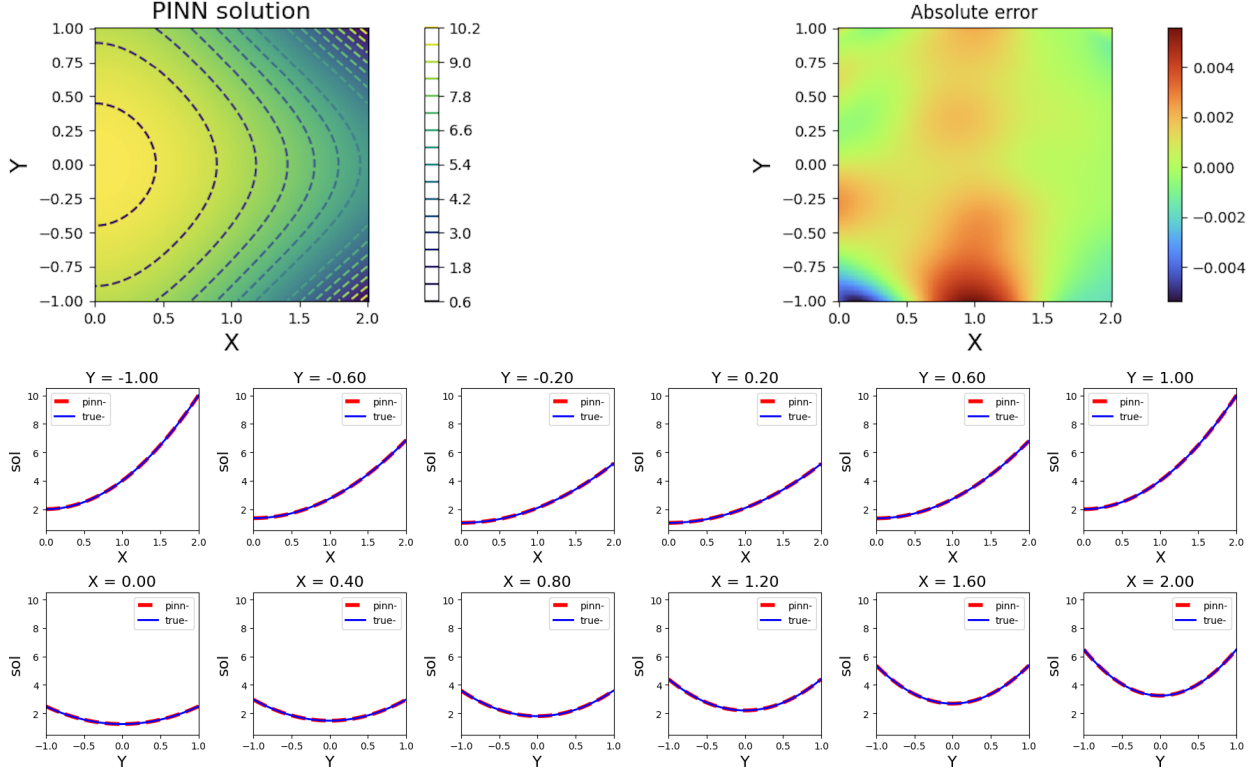


Figure 24: Predicted solution (iso-contours of  $\psi$  in top-left panel) of mathematical LE equation in a rectangular domain with Cauchy condition imposed at two boundaries ( $x = 0$ , and  $x = 2$ ). The absolute error is plotted in top-right panel. One dimensional cuts (at given  $y$  and  $x$  values) show the predicted solution versus the exact one.

is improved again. The latter result is clearly in Fig. 26, where the maximum absolute error is comparable to the first case with Cauchy condition imposed at the two opposite boundaries.

## 7.2 A physical example

In this subsection, we consider the problem related to the internal structure of a rotating self-gravitating gas sphere in hydrostatic equilibrium. In astrophysics, this is an approximation for different stars when a polytropic relation between the thermal pressure  $P$  and the gas density  $\rho$  is taken at any point inside the star, i.e.  $P = K\rho^{(1+1/n)}$  where  $n$  is a polytropic index having different values according to the type of star studied and  $K$  is a constant.

Using two physical equations, a first one related to the mass conservation (continuity equation) at any radius, and a second one related to equilibria between different forces (thermal pressure gradient force, gravitational force, and centrifugal force), one can recast the problem into a single second order differential equation that is the precisely the Lane-Emden equation. The latter can be written as

$$\Delta\psi + \psi^n = \omega, \quad (31)$$

where  $\Delta$  is the two dimensional spherical Laplacian operator  $\Delta = \frac{1}{r^2} \frac{\partial}{\partial r} (r^2 \frac{\partial}{\partial r}) + \frac{1}{r^2 \sin \theta} \frac{\partial}{\partial \theta} (\sin \theta \frac{\partial}{\partial \theta})$

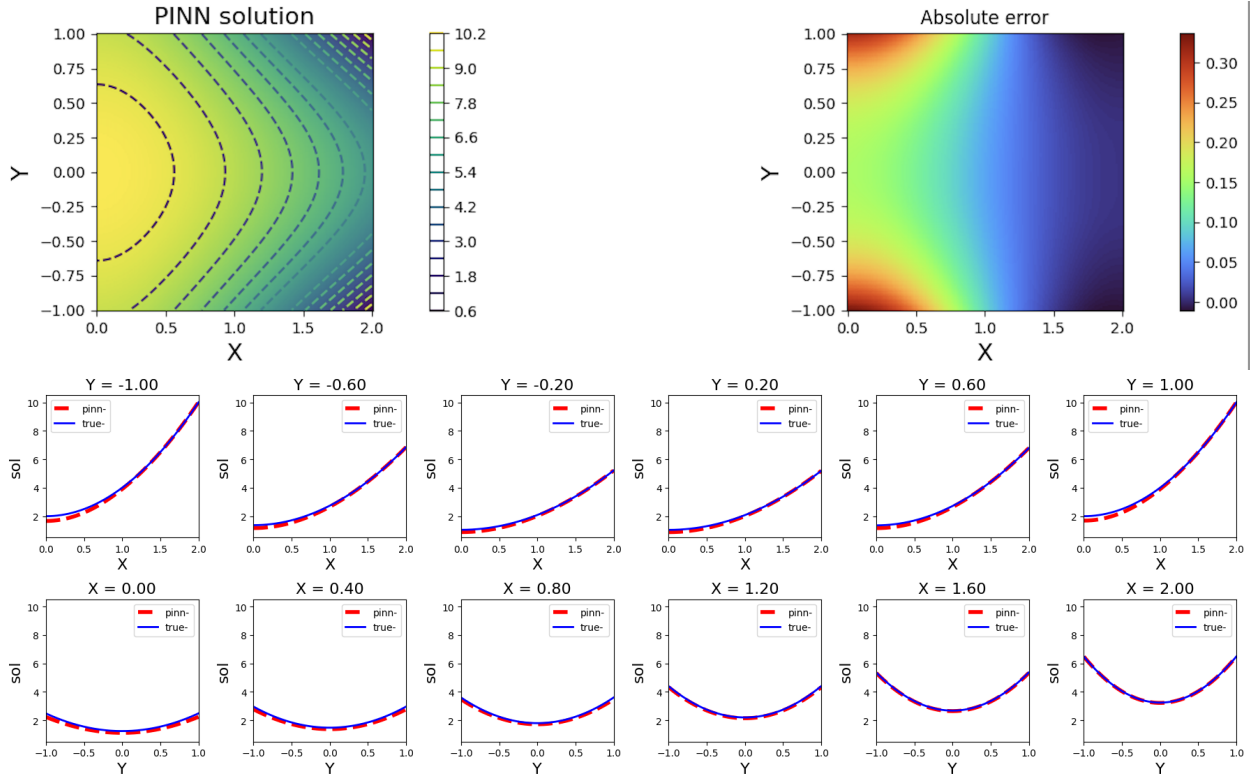


Figure 25: Same as in previous figure, but using Cauchy condition at only one boundary (i.e. at  $x = 2$ ).

and  $\omega$  is a constant representative of the rotation of the star (assumed to be uniform). Physically speaking,  $\psi$  is related to the mass density (see Baty 2023). For example, in the  $n = 1$  case, it is exactly the mass density normalized to the value at the center. This is a dimensionless equation depending on two spatial coordinates (spherical geometry) with  $r = R/R_c$  ( $R_c$  being the star radius) and with  $\theta$  the co-latitude angle varying between 0 and  $\pi$ . The problem is assumed axisymmetric and then does not depend on the remaining spherical angle. The latter can be also developed in the equivalent form (that is closer to the previous mathematical equation),

$$\frac{\partial^2 \psi}{\partial r^2} + \frac{2}{r} \frac{\partial \psi}{\partial r} + \frac{1}{r^2} \frac{\partial^2 \psi}{\partial \theta^2} + \frac{1}{r^2 \tan \theta} \frac{\partial \psi}{\partial \theta} + \psi^n = \omega. \quad (32)$$

However, contrary to the mathematical form (see Eq. 28), this physical form displays an obvious asymmetry between the two coordinates  $r$  and  $\theta$ .

We can solve the previous LE equation in the particular case  $n = 1$  without rotation (i.e.  $\omega = 0$ ). In this case, an analytical solution exists that is purely radial as  $\psi = \sin(r)/r$ . A PINN solver is developed using a PDE loss function based on the residual equation,

$$\mathcal{F} = r^2 \frac{\partial^2 \psi}{\partial r^2} + 2r \frac{\partial \psi}{\partial r} + \frac{\partial^2 \psi}{\partial \theta^2} + \frac{1}{\tan \theta} \frac{\partial \psi}{\partial \theta} + r^2 \psi^n = 0. \quad (33)$$

The BCs used in this problem are Cauchy condition on the axis  $r = 0$ , that are  $\psi = 1$  and  $\frac{\partial \psi}{\partial r} = 0$ .

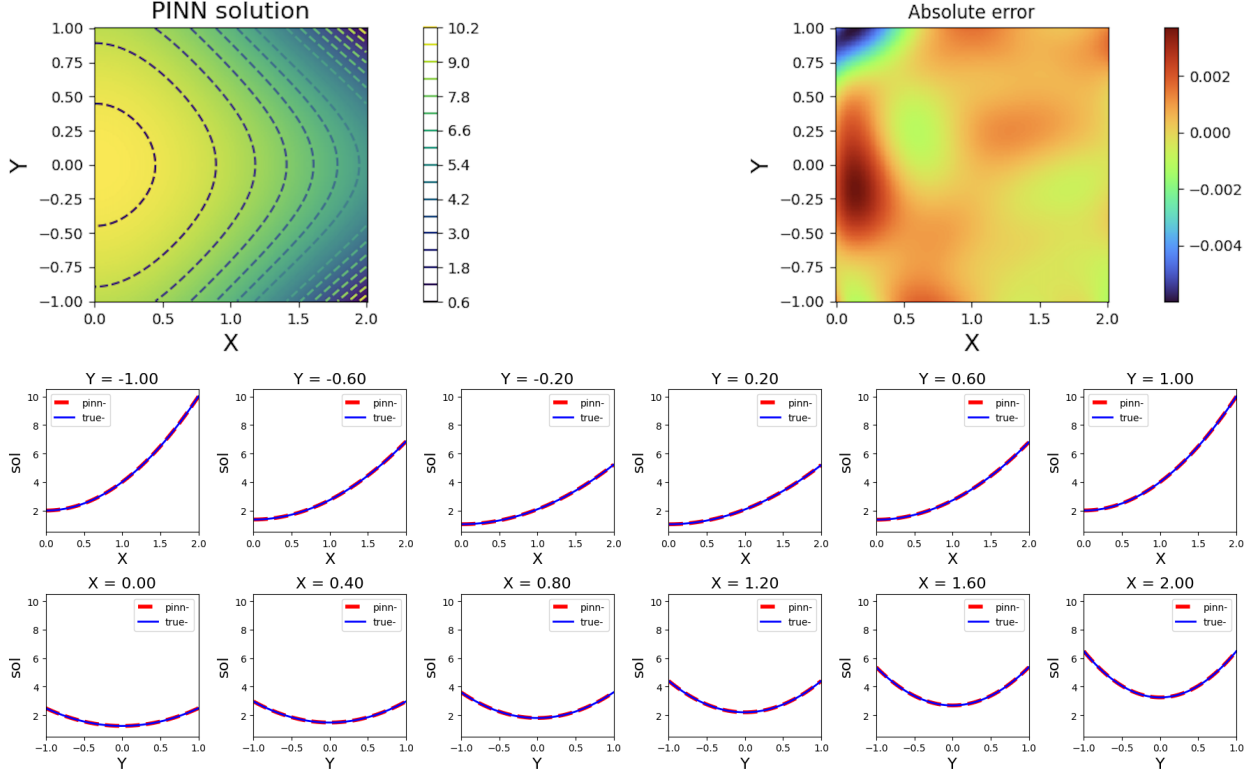


Figure 26: Same as in previous figure, but using Cauchy condition at only one boundary (i.e. at  $x = 2$ ) and Neumann condition at the two boundaries  $y \pm 1$ .

Neumann BCs are also added at the two boundaries  $\theta = 0, 2\pi$ , that are  $\frac{\partial \psi}{\partial \theta} = 0$ . Using 1000 collocation points randomly distributed in the domain  $\Omega = [0, \pi] \times [0, 2\pi]$  and 150 training data points at the three boundaries (50 per boundary), our PINNs solver is able to predict the exact solution with a precision similar to ones obtained for previous problems, as one can see in Figs 27-29. A total number of 70000 is used for this example.

Solutions for other index values (i.e.  $n$ ) can be also easily obtained in the same way. Note that, without rotation (i.e.  $\omega = 0$ ), the solutions are purely radial (see Baty 2023a). In principle this is not the case when the rotation factor is not zero, and a physically relevant solution should depend on the angle  $\theta$ . Unfortunately, the latter solution cannot be obtained using the Lane-Emden equation solely as some extra conditions are lacking (see Chandrasekhar & Milne 1938).

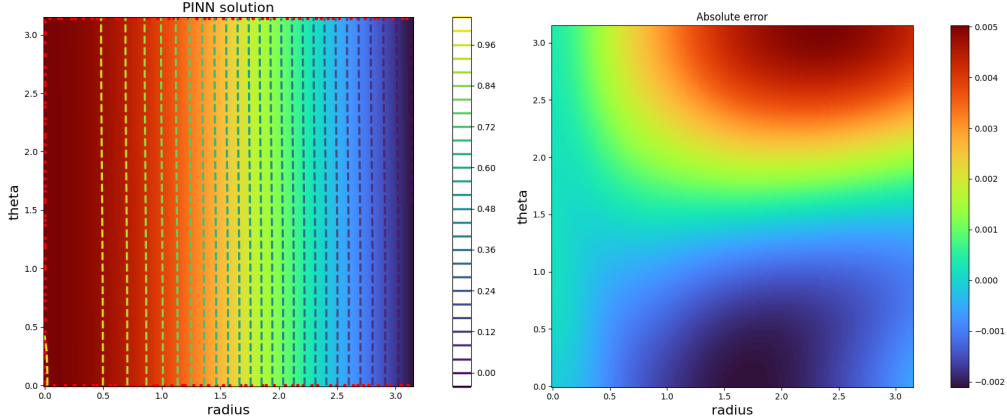


Figure 27: Predicted PINNs solution (left panel) and associated absolute error distribution (right panel) obtained from the physical Lane-Emden problem for  $n = 1$  and  $\omega = 0$  in the  $(r, \theta)$  plane.

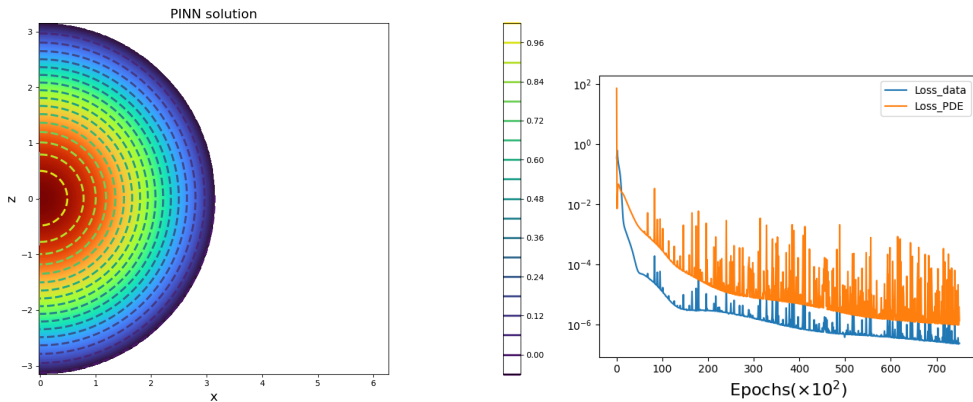


Figure 28: (Left panel) Predicted PINNs solution obtained from the physical Lane-Emden problem for  $n = 1$  and  $\omega = 0$  (see previous figure) plotted in the associated  $(z, x)$  plane. (Right panel) Evolution of the losses during the training process.

## 8 Parametric differential equation

### 8.1 Parametric solution for stationary advection diffusion in one dimension

In order to illustrate a PINNs solver aiming at learning multiple solutions of a given problem, we consider a simple differential equation residual (written in a residual form) as follows

$$c \frac{\partial u}{\partial x} - \mu \frac{\partial^2 u}{\partial x^2} - 1 = 0, \quad (34)$$

where  $u(x)$  is the desired solution in a one dimensional spatial domain with  $x$  in the range  $[0, 1]$ . As  $\mu$  is a dissipation coefficient (i.e. viscosity), and  $c$  is a constant coefficient analog to a velocity (taken to be unity for simplicity), the latter equation represents a steady-state advection-diffusion problem with the additional constant source term (i.e. unity). An example of exact solution with

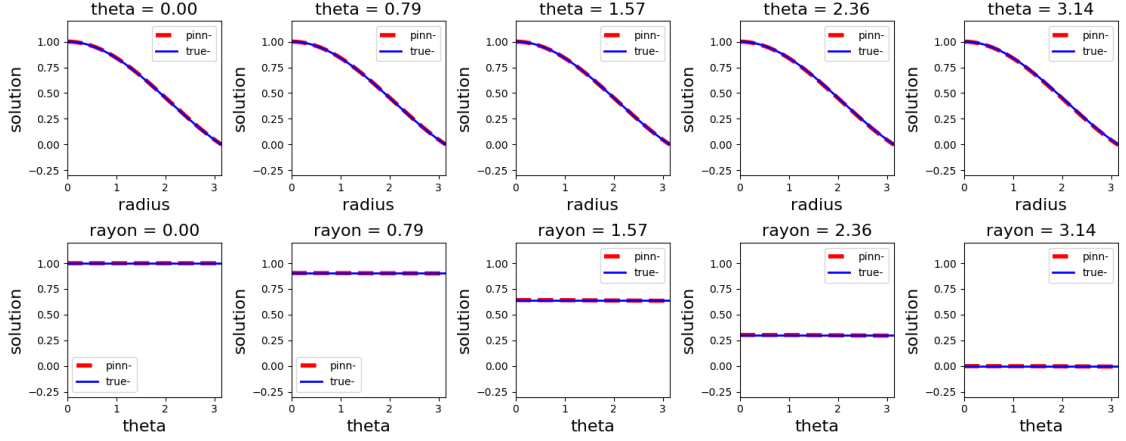


Figure 29: One dimensional cuts (at given  $r$  and  $\theta$  values) showing the predicted solution versus the exact one.

boundary conditions  $u(0) = u(1) = 0$  is

$$u(x) = x - \left[ \frac{e^{(x-1)/\mu} - e^{-1/\mu}}{1 - e^{-1/\mu}} \right]. \quad (35)$$

Such solution is known to involve the formation of singular layers (i.e. at  $x = 1$ ) when the viscosity employed is too small. As we are interested by learning the solutions at different viscosities with the same neural network, we can consider now variable  $\mu$  values taken in the range  $[0.1, 1.1]$ . A PINNs solver can thus be easily designed where the second neuron (see Fig. 5) corresponds now to  $\mu$  values, and the desired solution must be properly called now  $u(x, \mu)$ . The corresponding residual equation form is now

$$\mathcal{F}[u(x, \mu), x, \mu] = 0. \quad (36)$$

We can generate random distributions of training boundary points (typically 20 points at  $x = 0$  and 20 points at  $x = 1$  corresponding to different viscosity values in the range indicate above) and 400 collocation points in the  $(x, \mu)$  space  $\Omega = [0, 1] \times [0.1, 1.1]$  as one can see in Fig. 30. The exact boundary values (i.e. with zero values in the present problem) are imposed at these boundaries in order to minimize the training data loss function  $L_{data}$ , and the residual equation is evaluated on the collocation points for the variable viscosity in order to minimize the physics-based loss function  $L_{PDE}$ . The results are plotted in Fig. 31 (iso-contours in the trained plane) and Fig. 32 (cuts at different viscosity value) where one can see the predicted PINNs solution agrees very well with the exact one whatever the  $\mu$  value, with an error similar to values reported for the previous problems.

## 8.2 Stiff problems involving singular layers

Advection-diffusion equations, as considered in this section, generally involve singular layers (e.g. at the domain boundary as shown in the previous problem at  $x = 1$ ) that are particularly stiff as the diffusion coefficient is small. More exactly, the relevant parameter is the Reynolds number  $R_e = c/\mu$  which makes the problem stiff when it is much greater than unity. This causes numerical difficulties with PINNs, as it is also the case when employing traditional numerical methods (Baty 2023c).

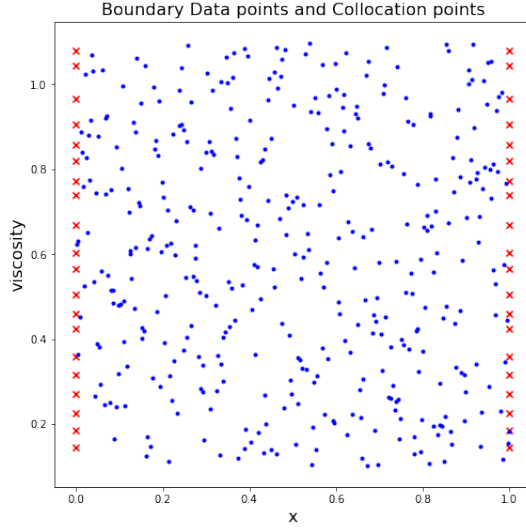


Figure 30: Scatter plot of the collocation points (blue dots) and of the training data (red crosses at the two boundaries  $x = 0, 1$ ) in the  $(x, \mu)$  plane.

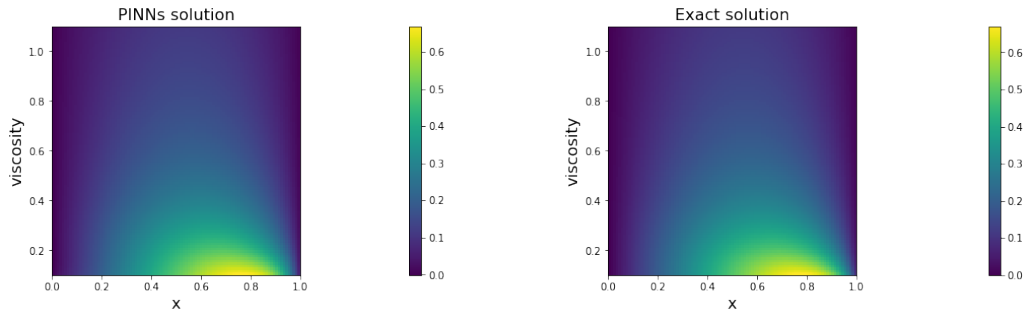


Figure 31: Colored iso-contours of the predicted PINNs solution  $u(x, \mu)$  and exact solution in the left and right panel respectively.

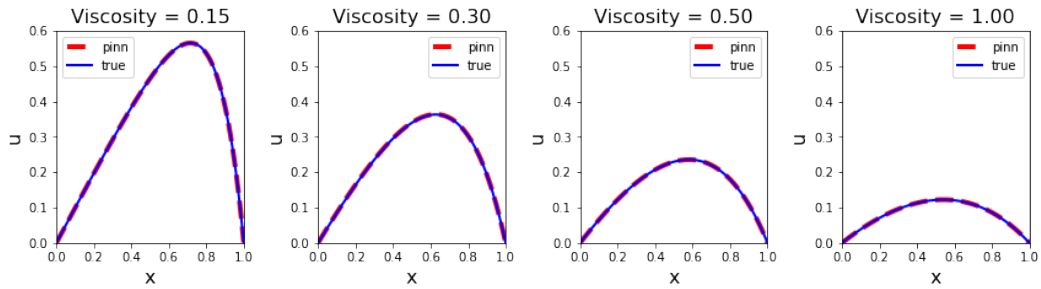


Figure 32: One-dimensional solution (red color) obtained for four different  $\mu$  viscosity values situated in the range of learned values (see legend) compared with the exact analytical solution (blue color), corresponding to one-dimensional cut obtained from previous figure.

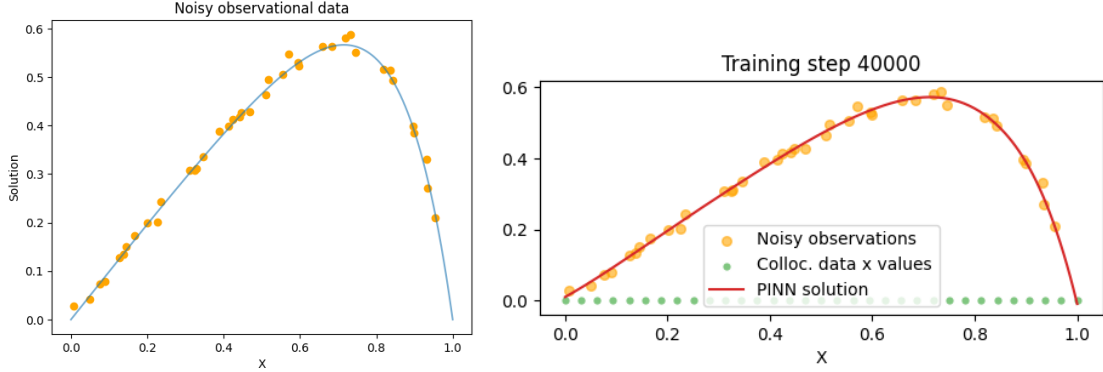


Figure 33: (Left panel) Set of data generated at different  $x$  values for a viscosity parameter  $\mu = 0.15$  from the expression Eq. 34 with additional random noise amplitude value 0.01. (Right panel) Predicted PINNs solution obtained at the end of the training process (after 40000 epochs).

As an interesting potential use of PINNs method, one can use hard-PINNs solver where a formulation close to Lagaris one (Lagaris 1998) allows to well capture the boundary layer solution at decreasingly small viscosity values. More explicitly, this is obtained by using a trial function having a exponential decay as  $\exp(-x/\mu)$  as it is the case for the exact solution at the singular boundary. The latter algorithm is named semi-analytic PINN method (Gie et al. 2024).

## 9 Inverse problem differential equation: parameter identification

We consider the same advection-diffusion equation as taken in the previous section (see Eq. 33). However, we are now interested in finding the unknown value for the viscosity coefficient  $\mu$ , from the knowledge of the equation together from a training data set giving the solution at these points (i.e. at some  $x$  values).

For example, using Eq. 35 (exact solution) we have generated some values (i.e. 40) at different  $x$  values (randomly distributed in the range  $[0, 1]$ ) for a given viscosity parameter that is  $\mu = 0.15$ . Moreover, in order to mimic data taken from measurements, we have added some random noise with an amplitude of 0.01 (see left panel of Fig. 33).

Our PINN solver is developed following the algorithm schematized in Fig.5. The aim is to use a PDE loss where the coefficient  $\mu$  is not a priori known and must be discovered/identified during the training process. The learning algorithm is similar to the non linear approximation scheme (Fig. 1) in the sense that, now the training data set not only consists in the initial/boundary data. Moreover, a number of 33 collocation points uniformly distributed in the whole interval are chosen in order to evaluate the PDE loss. As a result, at the end of the training (i.e. after 40000 epochs), the solution predicted by the PINN solver is plotted in right panel of Fig. 33. The later is similar to the solution used to generate the data using  $\mu = 0.15$ . We can also follow the estimation of the  $\mu$  parameter during the training as a function of the number of epochs. The result is plotted in Fig. 34 (left panel), showing that it rapidly converge to a value close to the (exact) expected value of 0.15 after 5000 epochs. More precisely, a value that is slightly smaller is obtained due to the noise effect. This is confirmed by the result using training data without noise, as one can see in right panel of Fig. 34.

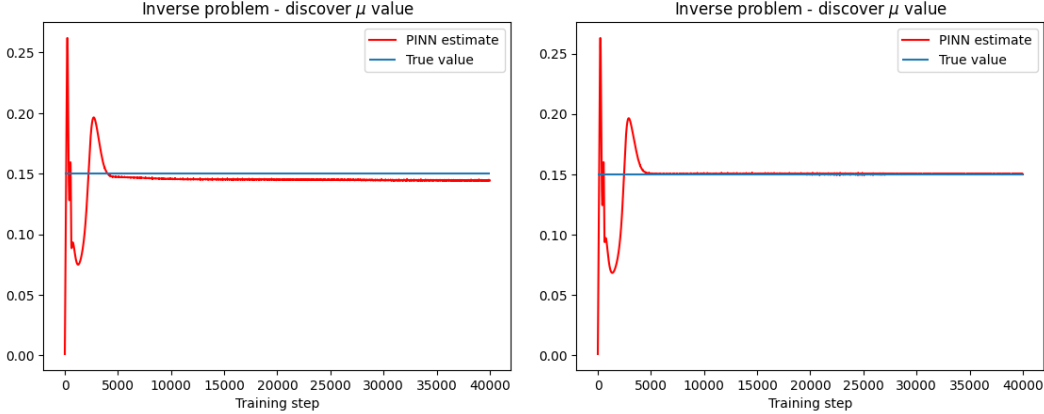


Figure 34: (Left panel) The viscosity parameter value  $\mu$  estimated by the PINNs solver during the training process, corresponding to the noisy data with a noise amplitude of 0.01 (see previous figure). (Right panel) The viscosity parameter value  $\mu$  estimated by the PINNs solver during the training process, corresponding to training data without noise.

## 10 Discussion and conclusion

In this work, we have introduced the basic concepts of using neural networks in order to solve 2D partial integrate differential equations via the use of PINNs.

Benchmark tests on different second order PDEs are taken in order to illustrate the putting into practice. Very simple problems based on Laplace and Poisson equations allowed to illustrate the use of vanilla-variant (soft boundary BCs with trainig data set) versus hard-variant (hard BCs via Lagaris-like method). The latter problems are also used to show how different types of BCs can be imposed in PINNs solver. More complex examples of PDEs taken from astrophysics are also considered. This is the case of Helmholtz equation for MHD modelling of magnetic arcades equilibria in the solar corona. This is also the case of Grad-Shafranov equation for MHD modelling the structures of curved loops. For the latter problems, PINNs solvers can easily deal with singularities (e.g. the singularity at  $r = 0$  for the physical Lane-Emden equation). Note that, PINNs method can be also used to solve particularly a rather large set of 6 partial differential equations representative of steady MHD model, as successfully shown by Baty & Vigon (2024) in the context of magnetic reconnection process.

The main advantage of PINNs when compared to traditional numerical integration methods is its numerical simplicity. Indeed, there is no need of discretization, like in a finite-difference method for example. Additionally, The required number of collocation points in order to ensure the convergence of the training is not so high. The second advantage is that, once trained the solution is instantaneously predicted on any other given grid (that can be different from the collocation grid). This is not the case of traditional methods which generally require some additional interpolation from the computing grid.

Unfortunately, PINNs have however some drawbacks. The training process can be long for some problems. Indeed, this is related to the lack of general automatic procedure for a fine tuning of the hyper-parameters of the network in order to have an optimal convergence during the training. The rules for the choice of the network architecture are not well determined. As concerns the accuracy,

the precision is good but not as good compared to traditional schemes, and it can reveal insufficient for some problems.

Finally, PINNs can be particularly useful when solving parametric PDEs (as illustrated on parametric advection-diffusion ODE in this report). In a similar way, PINNs can solve inverse problems for which a coefficient (or a term) is not known and must be discovered.

## Acknowledgements

Hubert Baty thanks, V. Vigon (IRMA and INRIA TONUS tream, Strasbourg) for stimulating discussions on PINNs technique, J. Pétri (Strasbourg observatory) for quoting the possibility to solve Lane-Emden equations, and L. Baty (CERMICS, école des Ponts ENPC) for helping in the use of Python libraries and impromptu general discussions on neural networks.

## References

- [Baty & Baty (2023)] Baty H., Baty L. 2023, Preprint, <https://doi.org/10.48550/arXiv.2302.12260>
- [Baty (2023a)] Baty H. 2023, Astronomy and Computing, 44, 100734, <https://doi.org/10.1016/j.ascom.2023.100734>
- [Baty (2023b)] Baty H. 2023, Preprint, <https://doi.org/10.48550/arXiv.2307.07302>
- [Baty (2023c)] Baty H. 2023, Preprint, <https://doi.org/10.48550/arXiv.2304.08289>
- [Baty & Vigon (2024)] Baty H., Vigon V. 2024, Monthly Notices of the Royal Astronomical Society, Volume 527, Issue 2, Pages 2575–2584, <https://doi.org/10.1093/mnras/stad3320>
- [Baydin et al. (2018)] Baydin A.G., Pearlmutter B.A., Radul A.A., & Siskin J.M. 2018, Journal of Machine Learning Research, 18, 1, <https://doi.org/10.48550/arXiv.1502.05767>
- [Bencheikh (2023)] Bencheikh A. 2023, Advances in Mathematics, Scientific Journal 12, 805
- [Chandrasekhar & Milne (1933)] Chandrasekhar S. , Milne E.A., Monthly Notices of the Royal Astronomical Society, Volume 93, Issue 5, March 1933, Pages 390–406
- [Cerfon & Freidberg (2010)] Cerfon A.J., Freidberg J.P., Phys. Plasmas 17, 032502 (2010)
- [Cuomo et al. (2022)] Cuomo S., Di Cola V.S., Giampaolo F., Rozza G. Raissi, M., & Piccialli F. 2022, Journal of Scientific Computing, 92, 88
- [Deriaz et al. (2011)] Deriaz E., Despres B., Faccanoni G., Pichon Gostaf K., Imbert-Gérard L.M., Sadaka G., & Sart, R. 2011, ESAIM Proc., 32, 76
- [Gie et al. (2024)] Gie G.-M., Hong Y., Jung C.-Y. 2024, to appear in Applicable Analysis, <https://doi.org/10.1080/00036811.2024.2302405>
- [Itakagi et al. (2004)] Itakaki M., Kamisawada J., Oikawa S., Nucl. Fusion 44 (2004) 427–437
- [Jang et al. (2024)] Jang B., Kaptanoglu A., Pan R., Landreman M., Dorland W. 2024, <https://doi.org/10.48550/arXiv.2311.13491>

[Karniadakis et al. (2021)] Karniadakis G.E., Kevrekidis I.G., Lu L, Perdikaris P., Wang S., & Yang L. 2021, Nature reviews, 422, 440, <https://doi.org/10.1038/s42254-021-00314-5>

[(Lagaris(1998)] Lagaris E., Likas A., & DI Fotiadis L. 1998, IEEE transactions on neural networks, 9(5), 987

[(Nishikawa (2023)] Nishikawa H., <http://www.cfdbooks.com/>, <http://www.hiroakinishikawa.com/>

[Peng et al. (2020)] Peng Z., Tang Q., Pan R., Tang X.-Z. 2020, SIAM Journal on Scientific Computing Vol. 42, 5

[Press et al. (2007)] Press W.H., Teukolsky S.A., Vetterling W.T., & Flannery B.P. 2007, Numerical Recipes 3rd Edition

[Raissi et al. (2019)] Raissi M., Perdikaris P., & Karniadakis G.E. 2019, Journal of Computational Physics, 378, 686, <https://doi.org/10.1016/j.jcp.2018.10.045>

[Soloviev (1975)] Soloviev L.S. 1975, Reviews of Plasma Physics, 6, 239

[Urbán et al. (2023)] Urban J.F., Stefanou P., Dehman C., & Pons J.A. 2023, MNRAS, 524, 32, <https://doi.org/10.1093/mnras/stad1810>

## 11 Appendix

We have plotted in Figures 35 and 36, the results obtained when solving Poisson problems (equations b-e, see main text) with Dirichlet and Neumann BCs using vanilla-PINNs respectively.

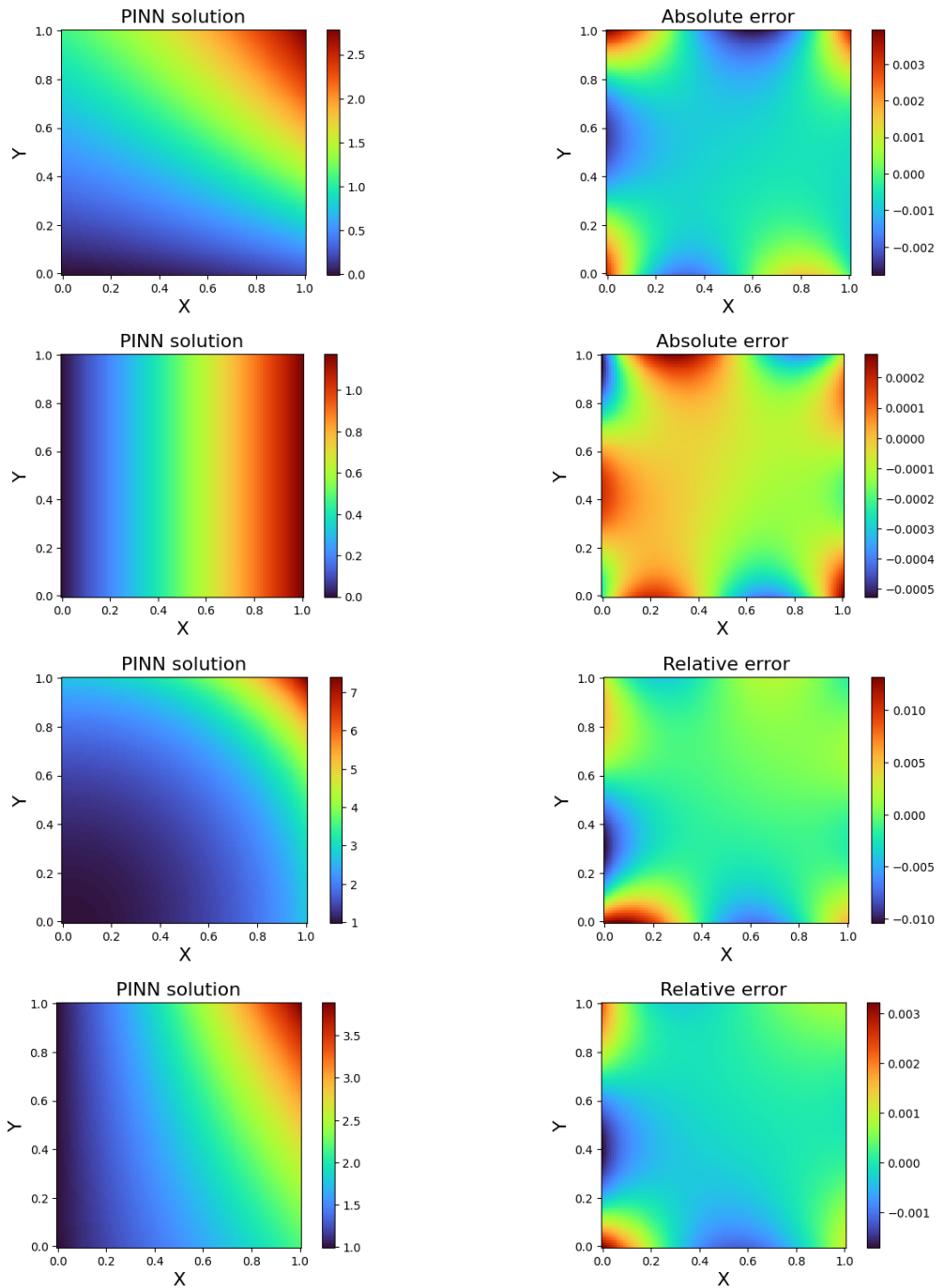


Figure 35: PINNs solution and corresponding absolute/relative error distribution as colored iso-contours corresponding to Poisson problem with Dirichlet BCs using vanilla-PINNs. The four equations (b-e) examples are considered from top to bottom panels respectively (see text).

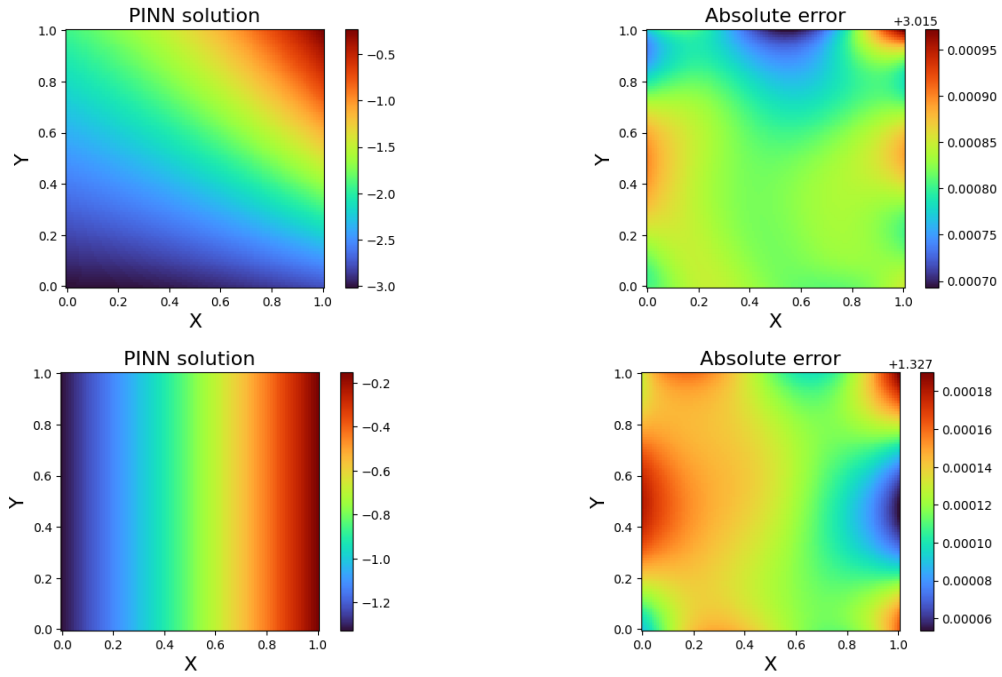


Figure 36: PINNs solution and corresponding absolute/relative error distribution as colored iso-contours corresponding to Poisson problem with Neumann BCs using vanilla-PINNs. The two equations (b-c) examples are considered from top to bottom panels respectively (see text).